Doklady Physics, Vol. 50, No. 8, 2005, pp. 389–392. Translated from Doklady Akademii Nauk, Vol. 403, No. 4, 2005, pp. 471–474.

PHYSICS

Thermodynamic Properties of Magnesium Silicates

N. A. Arutyunyan*, A. I. Zaitsev, N. E. Zaitseva**, and E. Kh. Shakhpazov*****

Presented by Academician N.P. Lyakishev February 8, 2005

Received February 9, 2005

Being a constituent of numerous minerals, magnesium silicates are of extraordinary interest for the Earth and planetary sciences, as well as for cosmology. At the same time, they have many industrial and technological applications, including those associated with the building industry. Reliable data on the thermodynamic properties of magnesium silicates at high temperatures are necessary for the forecasting of various natural phenomena, optimization of technological parameters in a wide range of technological processes and production techniques, and for the development of novel ceramic and ceramic-metal materials, glasses, fluxes, slags and slag-forming mixtures. However, these data are at present almost entirely absent. Results from the direct measurement of thermodynamic characteristics for a magnesium-silicate melt have been reported by a single group only [1, 2]. However, these results do not agree with the data related to the phase diagram [3]. The description of the thermodynamic characteristics of intermediate phases is mainly based on low-temperature measurements and the extrapolation of temperature dependence for specific heats [4].

The present study is aimed at determining the thermodynamic properties of all phases existing in the $MgO–SiO_2$ system within the wide temperature range 1571–1873 K for the entire set of chemical compositions. The measurements were performed by the Knudsen mass-spectrometry method using the approach of [5], which was based on the generation of volatile reaction products formed as a result of the reduction of oxide components. When the $MgO–SiO_2$ mixture interacts with the reducing agent R, which is, in this case, either the material of the effusion cell itself (R = Ta, Nb, Mo) or the purposefully added powders of these metals, the following chemical reactions occur:

$$n\mathrm{MgO(solid, liquid)} + \mathrm{R(solid)} = \mathrm{RO}_n\mathrm{(gas)} + n\mathrm{Mg(gas)}, \quad (1)$$

$$n\mathrm{SiO_2(solid, liquid)} + \mathrm{R(solid)} = \mathrm{RO}_n\mathrm{(gas)} + n\mathrm{SiO(gas)}. \quad (2)$$

The calculations and preliminary experiments performed have demonstrated that both processes (1) and (2) take place in liquid and crystallized $MgO–SiO_2$ mixtures. Hence, in order to determine the thermodynamic properties of the components, we can study the equilibrium conditions for the chemical reaction

$$\mathrm{SiO_2(solid, liquid)} + \mathrm{Mg(gas)} = \mathrm{MgO(solid, liquid)} + \mathrm{SiO(gas)}. \quad (3)$$

The $MgO–SiO_2$ compositions were synthesized using high purity MgO and SiO_2 preliminarily dried by heating in vacuum. Some samples were produced directly in the effusion chamber, whereas others were manufactured by melting the components together in closed molybdenum crucibles in a vacuum not worse than 10^{-4} Pa with subsequent long-time homogenizing annealing. The selective chemical and X-ray phase analysis conducted after the measurements had been performed demonstrated that, in the course of the experiments, there occurred neither a significant dissolution of Nb, Ta, or Mo oxides, nor changes in the oxygen stoichiometry of MgO and SiO_2. In other words, the configuration point of the sample composition did not exceed the limits of the quasi-binary $MgO–SiO_2$ cut for the Mg–O–Si system. The X-ray diffraction patterns exhibited only such lines as corresponded to combinations of the equilibrium phases existing in the $MgO–SiO_2$ system.

The mass-spectrometry of saturated vapor that formed above the $MgO–SiO_2$ system revealed the existence of Mg^+, SiO^+, MoO^+, MoO_2^+, MoO_3^+, NbO^+, NbO_2^+, TaO^+, and TaO_2^+ ions arising as a result of the ionization of Mg, SiO, MoO, MoO_2, MoO_3, NbO,

* *Moscow State University, Vorob'evy gory, Moscow, 119899 Russia*

** *Kurdyumov Institute of Metallography and Metal Physics, Associated with Bardin Central Research Institute for the Iron and Steel Industry, Vtoraya Baumanskaya ul. 9/23, Moscow, 107005 Russia*

*** *Baĭkov Institute of Metallurgy and Materials Science, Russian Academy of Sciences, Leninskiĭ pr. 49, Moscow, 119334 Russia*

1028-3358/05/5008-0389$26.00

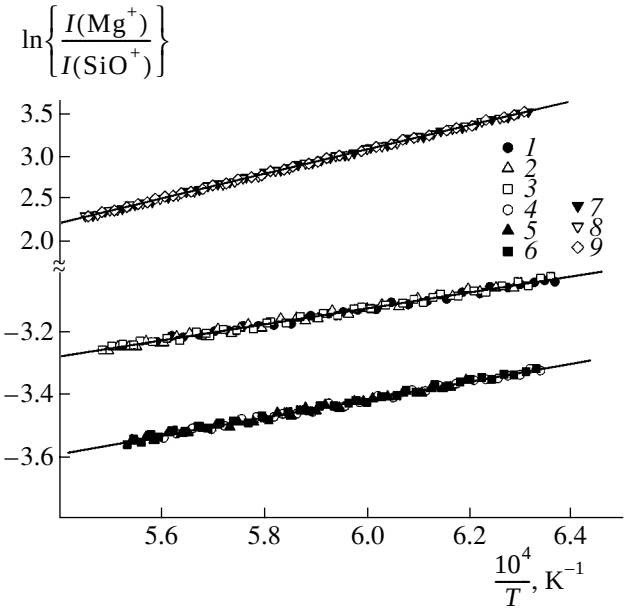

Fig. 1. Temperature dependence of $\ln\left\{\frac{I(Mg^+)}{I(SiO^+)}\right\}$ determined for $MgO–SiO_2$ crystalline mixtures of different chemical composition, which were measured under different experimental conditions, i.e., different values $x(SiO_2)$, material of the effusion chamber, and diameter d_{eff} (mm) of the effusion hole: (*1*) 0.498, Nb, 0.162; (*2*) 0.486, Ta, 0.190; (*3*) 0.403, Mo, 0.284; (*4*) 0.605, Nb, 0.154; (*5*) 0.563, Ta, 0.181; (*6*) 0.528, Mo, 0.232; (*7*) 0.678, Nb, 0.129; (*8*) 0.745, Ta, 0.157; and (*9*) 0.811, Mo, 0.201.

NbO_2, TaO, and TaO_2 molecules. The most intense lines corresponded to Mg^+, SiO^+, MoO_2^+, NbO_2^+, and TaO_2^+ ions.

In the crystalline state of the $MgO–SiO_2$ system, there exist two intermediate phases having the metasilicate ($MgSiO_3$) and orthosilicate (Mg_2SiO_4) compositions. The determination of the intensity ratio $\frac{I(Mg^+)}{I(SiO^+)}$ for ionic currents in all heterogeneous mixtures enabled us to find the following expression for the partial Gibbs free energy of MgO and SiO_2 in the $MgSiO_3$–Mg_2SiO_4 two-phase region using the equilibrium constant for reaction (3):

$$\Delta_f G''(MgO) = \frac{RT}{3}\left\{\ln\frac{I''(Mg^+)}{I''(SiO^+)} - \ln\frac{I'(Mg^+)}{I'(SiO^+)}\right\}, \quad (4)$$

$$\Delta_f G''(SiO_2) = \frac{RT}{2}\left\{\ln\frac{I'''(Mg^+)}{I'''(SiO^+)} - \ln\frac{I''(Mg^+)}{I''(SiO^+)}\right\}. \quad (5)$$

Here, symbols marked by a single prime, two primes, and three primes correspond to heterogeneous fields MgO + Mg_2SiO_4, $MgSiO_3$ + Mg_2SiO_4, and $MgSiO_3$ + SiO_2, respectively. In each coexistence region for two crystal phases, we have studied several samples of different compositions. The intensity ratios for currents produced by Mg^+ and SiO^+ ions, which were measured under various experimental conditions (material of effusion chamber, diameter of the effusion hole), were highly reproducible. The maximum deviation did not exceed the experimental error (about 1%) of the determination of ionic currents, so that it was possible to perform the combined data processing (Fig. 1). Based on the coefficients for the temperature dependence $\ln\left\{\frac{I(Mg^+)}{I(SiO^+)}\right\} = \frac{A}{T} + B$ (Table 1), which were determined by the least-squares method, we have calculated according to expressions (4) and (5) the partial Gibbs free energies (expressed in J/mol) for MgO and SiO_2 in heterogeneous fields $MgSiO_3$ + Mg_2SiO_4 using as reference points the corresponding values for crystalline MgO and β-cristobalite:

$$\Delta_f G''(MgO) = –(32144 \pm 245) + (2.15 \pm 0.16)T, \quad (6)$$

$$\Delta_f G''(SiO_2) = (1302 \pm 332) + (2.01 \pm 0.24)T. \quad (7)$$

The partial thermodynamic parameters determined for both components of the heterogeneous mixture of magnesium metasilicate and orthosilicate allowed us to calculate (and to express in units of J/mol) the integral thermodynamic functions related to the formation of these compounds:

$$\Delta_f G(MgSiO_3) = –(30842 \pm 413) + (0.14 \pm 0.29)T, \quad (8)$$

$$\Delta_f G(Mg_2SiO_4) = –(62986 \pm 592) + (2.19 \pm 0.40)T. \quad (9)$$

The dependence of x(MgO) on $\ln\left\{\frac{I(Mg^+)}{I(SiO^+)}\right\}$ determined from the experimental data for $MgO–SiO_2$ melt has a complicated form (Fig. 2). The sharp breaks observed correspond to the positions of stability boundaries for the liquid phase. The performed calculations

Table 1. Parameters of temperature dependences for the intensity ratios $\ln\left\{\frac{I(Mg^+)}{I(SiO^+)}\right\} = \frac{A}{T} + B$ of ionic currents above the $MgO–SiO_2$ crystalline mixture

Phase field	T, K	n	$A \pm \Delta A$	$–B \pm \Delta B$
MgO + Mg_2SiO_4	1584–1835	95	14190 ± 68	5.455 ± 0.040
$MgSiO_3$ + Mg_2SiO_4	1571–1824	95	2592 ± 56	4.680 ± 0.040
$MgSiO_3$ + SiO_2	1578–1808	92	2905 ± 57	5.164 ± 0.040

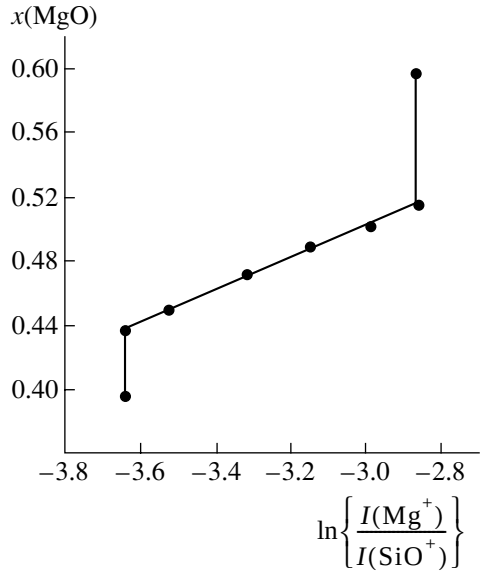

Fig. 2. Dependence of x(MgO) on $\ln\left\{\frac{I(Mg^+)}{I(SiO^+)}\right\}$ (T = 1873 K).

yielded the values $x^l(SiO_2)$ = 0.488 and 0.563 (T = 1873 K) for the liquidus positions from the side of magnesium silicate and silica, respectively. These values are in good agreement with the published data on the phase diagram: $x^l(SiO_2)$ = 0.494 and 0.562 (T = 1873 K) [3]. The activities of the components in the liquid phase were determined by integrating the Gibbs–Duhem equation expressed in terms of the intensity ratio for ionic currents. For example, the activity of MgO in the MgO–SiO_2 melt is calculated on the basis of the relationship

$$\ln a(\mathrm{MgO}) = -\int_{x(\mathrm{MgO})=x^l(\mathrm{MgO})}^{x(\mathrm{MgO})} x(\mathrm{SiO_2})\,d\ln\frac{a(\mathrm{SiO_2})}{a(\mathrm{MgO})} = -\int_{x(\mathrm{MgO})=x^l(\mathrm{MgO})}^{x(\mathrm{MgO})} x(\mathrm{SiO_2})\,d\ln\left(\frac{I(Mg^+)}{I(SiO^+)}\right). \quad (10)$$

The initial value a(MgO) in the equilibrium region between the melt and Mg_2SiO_4 was calculated using Eq. (9) and the found value $a(SiO_2)$. The results obtained are presented in Table 2.

The concentration dependences of thermodynamic functions related to the formation of crystalline MgO–SiO_2 mixtures have asymmetric shapes (Fig. 3). The extrema of the corresponding curves are shifted toward MgO and their positions correspond to the forsterite composition (Mg_2SiO_4). This well agrees with the shape of the MgO–SiO_2 phase diagram [3]. For comparison, we present in Fig. 3 the values of the Gibbs

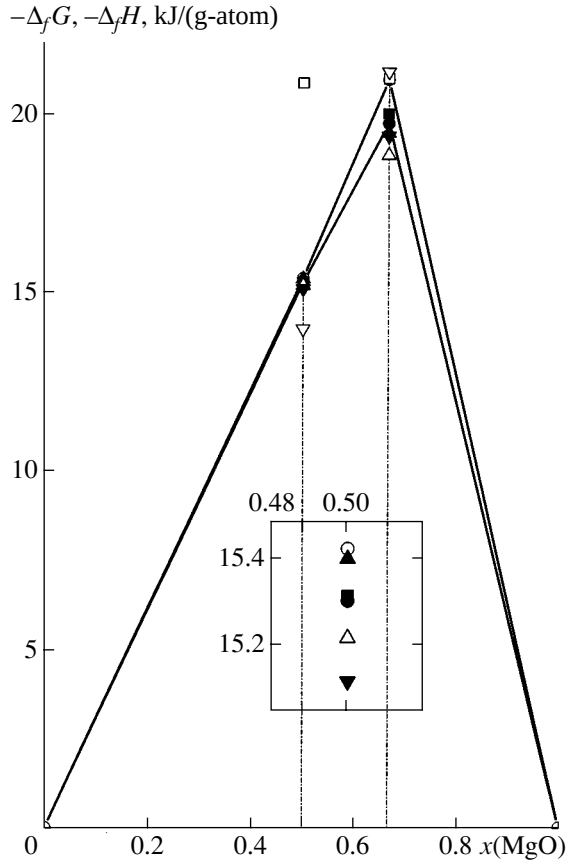

Fig. 3. Thermodynamic functions that characterize the formation of magnesium silicates (T = 1700 K) from β-cristobalite and crystalline MgO. The results of the present study: (●) $\Delta_f G$ and (○) $\Delta_f H$. The data of other authors: (■) $\Delta_f G$ and (□) $\Delta_f H$ [6]; (▲) $\Delta_f G$ and (△) $\Delta_f H$ [4]; (▼) $\Delta_f G$ and (▽) $\Delta_f H$ [7].

free energy $\Delta_f G$ and enthalpy $\Delta_f H$ for protoenstatite $MgSiO_3$ and forsterite, which are given in the reference book [6] and reported in [4, 7]. These values were found by means of the combined analysis (optimization) of all available data on the thermodynamic prop-

Table 2. Activities of the components in the MgO–SiO_2 melt with respect to β-cristobalite and crystalline MgO (T = 1873 K)

$x(SiO_2)$	$a(SiO_2)$	a(MgO)
0.486*	0.693	0.181
0.498	0.737	0.171
0.511	0.797	0.158
0.528	0.865	0.144
0.550	0.951	0.129
0.563	1.0	0.122

* The coexistence region for the melt and Mg_2SiO_4.

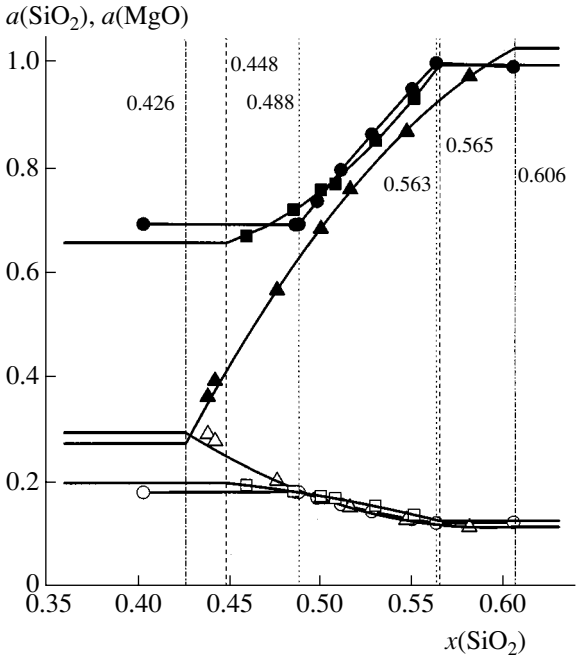

Fig. 4. Activities of components forming $MgO–SiO_2$ melt at T = 1873 K. Data of the present study: (●) $a(SiO_2)$ and (○) $a(MgO)$. Data of other authors: (■) $a(SiO_2)$ and (□) $a(MgO)$, T = 1873 K [1]; (▲) $a(SiO_2)$ and (△) $a(MgO)$, T = 1973 K [2].

erties and phase equilibrium conditions in the $MgO–SiO_2$ system. The analysis was focused on finding the most precise and justified values of the parameters that characterize these two types of data. One can see that the values $\Delta_f G$ reported in all the papers are close to each other, whereas there is a substantial divergence of the data for $\Delta_f H$. The value of $\Delta_f H(MgSiO_3)$ recommended in the reference book [6] seems to be too low. This implies that the chemical bonds in magnesium orthosilicate and metasilicate are comparable in terms of strength, which is difficult to reconcile with the incongruent melting type of the latter silicate [3]. In contrast, the enthalpy change corresponding to the formation of forsterite from the components found in [4] turns out to be too low. The described situation probably stems from the absence of direct measurements of thermal parameters characterizing the formation of magnesium silicates at high temperatures. Therefore, it is necessary to extrapolate the quantities measured at relatively low temperatures to a wider temperature range.

The activities of the components forming the $MgO–SiO_2$ melt, which were determined in the present study and in the studies [1, 2], are close to each other (Fig. 4), but they differ in the shape of their concentration dependence. In [1, 2], the existence of a much broader stability range for the liquid phase at 1873 K and 1973 K was reported than follows from the data of [3] on the phase diagram (the reported range is extended to the region in which the formation of magnesium orthosilicate occurs). In the liquid $MgO–SiO_2$ mixtures, it is this composition range that is characterized by the most pronounced tendency to glass formation [8, 9]. Apparently, in the course of the measurements performed in [1, 2], the supercooling of the melt was not avoided, and this has led to a certain distortion in the concentration functions of the activity.

Thus, in the present study, the thermodynamic properties of liquid and crystalline $MgO–SiO_2$ compositions were determined by means of measurements performed with several samples of both the same and different compositions under different experimental conditions. In all the cases, the measured values for the ratios of ionic-current intensities coincided with each other within the experimental errors (about 1%). Therefore, it was possible to perform the combined treatment of these data (see Tables 1 and 2). We also note that none of the calculation methods that were used required data on the ionization cross sections of gas molecules or on the sensitivity of the mass-spectrometric device. This has led to a substantial enhancement of the determination accuracy of the thermal parameters. All of this allows us to recommend the obtained data for use in the thermodynamic calculations of reactions and processes involving $MgO–SiO_2$ mixtures and, in particular, for choosing slags and slag-forming mixtures for the continuous casting of steels with improved operating performance.

ACKNOWLEDGMENTS

This work was supported by the Russian Foundation for Basic Research, project no. 04-03-08147.

REFERENCES

1. S. Kambayashi and E. Kato, J. Chem. Thermodyn. **15**, 701 (1983).
2. S. Kambayashi and E. Kato, J. Chem. Thermodyn. **16**, 241 (1984).
3. *Atlas of Slags. Reference Book* (Metallurgiya, Moscow, 1985) [in Russian].
4. M. Hillert and X. Wang, Calphad **13** (3), 253 (1989).
5. A. I. Zaitsev and B. M. Mogutnov, J. Mater. Chem. **5** (7), 1063 (1995).
6. *JANAF Thermochemical Tables*, J. Phys. Ref. Data **14** (1985).
7. P. Wu, G. Erikson, A. Pelton, *et al.*, ISIJ Intern. **33** (1), 26 (1993).
8. S. A. Dembovskiĭ and E. A. Chechetkina, *Glass Formation* (Nauka, Moscow, 1990) [in Russian].
9. A. I. Zaitsev and N. E. Zaitseva, Izv. Akad. Nauk, Ser. Fiz. **65** (10), 1390 (2001).

Translated by K. Kugel

Doklady Physics, Vol. 50, No. 8, 2005, pp. 393–396. Translated from Doklady Akademii Nauk, Vol. 403, No. 4, 2005, pp. 475–477.

PHYSICS

Determination of the Form of the Grüneisen Coefficient for Molecular Crystals

Yu. M. Kovalev

Presented by Academician B.V. Litvinov January 27, 2005

Received January 27, 2005

Determination of the Grüneisen coefficient as a function of the specific volume is one of the basic problems in constructing equations of state for solids. Many theoretical and experimental studies have been devoted to solving this problem [1–3]. However, in the case of molecular crystals, the problem is especially complicated by virtue of the fact that molecules composing a crystal possess a large number of degrees of freedom. Nevertheless, the present author has managed to overcome this difficulty and has obtained in analytical form the dependence of the Grüneisen coefficient on the specific volume of a solid, which was precisely the goal of this paper.

The thermodynamic properties of a substance can be entirely determined provided that one of the thermodynamic potentials is known. It is convenient to proceed from the definition of the Helmholtz free energy $F(V, T)$, which is most simply formulated in association with a model of the substance structure:

$$F = u + E_0 + kT\sum_{\alpha}\ln\left[1 - \exp\left(-\frac{h\omega_\alpha}{kT}\right)\right], \qquad E_0 = \frac{1}{2}\sum_{\alpha}h\omega_\alpha. \tag{1}$$

Here, u is the energy of interatomic interaction, V is the specific volume, T is temperature of a body, k is the Boltzmann constant, h is the Planck's constant, ω_α is the frequency of normal oscillations, and E_0 is the energy of zero oscillations.

If $F(V, T)$ is specified, then the expressions for all measurable thermodynamic quantities can be found by differentiation:

$$S = -\left(\frac{\partial F}{\partial T}\right)_V, \quad P = -\left(\frac{\partial F}{\partial V}\right)_T, \quad \left(\frac{\partial S}{\partial V}\right)_T = \left(\frac{\partial P}{\partial T}\right)_V. \tag{2}$$

It is well known that the interaction energy between atoms of a molecular crystal is the sum of the intramolecular and intermolecular energies. The former consists of the energies of the valent and non-valent interactions of atoms inside a molecule. The intermolecular energy is that of the non-valent interactions of atoms belonging to different molecules. It is well known that the intramolecular energy of valent interactions considerably exceeds the energy of non-valent interactions between atoms both inside a molecule and amongst atoms of different molecules. Therefore, it is reasonable to divide the interaction energy of a molecular crystal into the molecular energy u_M (energy of valent interactions) and crystal energy u_C (energy of non-valent interactions). If the energy u_C is dependent on the spatial disposition of molecules, then the energy u_M exceptionally depends on values of valent bonds and valent angles.

It is well known that the frequencies of normal oscillations inside a molecule exceed by an order of magnitude those of normal oscillations for a molecule as a whole and also of deformation oscillations. With allowance for this fact, we can introduce two characteristic temperatures and divide the oscillatory component of the free energy into low-frequency and high-frequency parts. The frequencies of normal oscillations of a molecule as a whole and of deformation oscillations are determined by the variation of the energy u_C, i.e., by the energy of non-valent interactions. Therefore, only these frequencies of normal oscillations depend on the volume.

Assuming that the Debye (Einstein) approach is valid in application to the low-frequency (high-frequency) component of the free energy, we can rewrite expression (1) in the form

$$F = u_C + u_M + E_0 + 3MRT\left(\frac{T}{\theta_D}\right)^3 \times \int_0^{\theta_D/T}\xi^2\ln[1 - \exp(-\xi)]d\xi + (3N - M)RT\ln\left[1 - \exp\left(-\frac{\theta_E}{T}\right)\right]. \tag{3}$$

Chelyabinsk State University,
ul. Brat'ev Kashirinykh 129, Chelyabinsk, 454021 Russia
e-mail: kovalev@cgu.ru

1028-3358/05/5008-0393$26.00

Here, R is the universal gas constant, M is the number of low-frequency oscillations, N is the number of atoms in a molecule, $3N - M$ is the number of high-frequency oscillations, θ_D is the Debye characteristic temperature, and θ_E is the Einstein characteristic temperature.

Upon integrating by parts the expression for the low-frequency component $F(V, T)$ of the free energy and introducing the Debye function $D(x)$ in accordance with formulas presented in monographs [4, 5], namely,

$$D(x) = \frac{3}{x^3}\int_0^x \xi^3 \frac{d\xi}{\exp\xi - 1},$$

we arrive at

$$F = u_M + u_C + E_0 + MRT\left[\ln(1 - \exp(-x_D)) - \frac{D(x_D)}{3}\right] + (3N - M)RT\ln[1 - \exp(-x_E)], \quad (4)$$

where $x_D = \dfrac{\theta_D}{T}$ and $x_E = \dfrac{\theta_E}{T}$.

Using formula (3), we easily obtain the expression for the pressure P and entropy S:

$$P = -\left(\frac{\partial F}{\partial V}\right)_T = -\frac{\partial u_M}{\partial V} - \frac{du_C}{dV} - \frac{dE_0}{dV} - MRTD(x_D)\frac{d\ln\theta_D}{d\ln V}\frac{1}{V} - (3N - M)RTx_E\frac{d\ln\theta_E}{d\ln V}\frac{1}{V(\exp x_E - 1)}, \quad (5)$$

$$S = -\left(\frac{\partial F}{\partial V}\right)_T = -\left\{MR\left[\ln(1 - \exp(-x_D)) - \frac{D(x_D)}{3}\right] - MRD(x_D) + (3N - M)R\ln[1 - \exp(-x_E)] - \frac{(3N - M)RTx_E}{\exp x_E - 1}\right\}. \quad (6)$$

In deriving formula (6), we have used the following feature of the Debye function:

$$D(x) = \frac{x}{\exp x - 1} - \frac{x}{3}D'(x), \quad (7)$$

where the symbol prime corresponds to differentiation over the characteristic temperature x.

With known equalities (4) and (6), it is easy to determine expressions for the total energy and heat capacity C_V at the constant volume:

$$E = F + TS = u_M + u_C + E_0 + MRTD(x_D) + \frac{(3N - M)RTx_E}{\exp x_E - 1}, \quad (8)$$

$$C_V = MR\left[4D(x_D) - \frac{3x_D}{\exp x_D - 1}\right] + \frac{(3N - M)Rx_E^2\exp x_E}{(\exp x_E - 1)^2}. \quad (9)$$

Following the definition of the Grüneisen coefficient

$$\gamma_D(V) = -\frac{d\ln\theta_D}{d\ln V}, \quad (10)$$

we can rewrite expression (5) in the form

$$P = -\frac{\partial u_M}{\partial V} - \frac{\partial u_C}{\partial V} - \frac{dE_0}{dV} + \frac{MRT\gamma_D(V)D(x_D)}{V}. \quad (11)$$

The last term in expression (5) equals zero because, while dividing frequencies, we have made the assumption that high frequencies are volume-independent.

Thus, based on the definition of the zero-oscillation energy and allowing for the separation of frequencies, we arrive at the expression for the function E_0 and $\dfrac{dE_0}{dV}$:

$$E_0 = \frac{1}{2}\sum_\alpha h\omega_\alpha = \frac{3N' - M'}{2}h\omega_E + \frac{3M'}{2}\int_0^{\omega_D}\omega^2 h\omega\, d\omega = \frac{3N - M}{2}R\theta_E + \frac{3}{8}MR\theta_D(V), \quad (12)$$

$$\frac{dE_0}{dV} = -\frac{3}{8}\frac{MR\gamma_D(V)\theta_D}{V}. \quad (13)$$

Here, N' and M' are the numbers of atoms and of low-frequency oscillations in the volume V, respectively.

Substituting the expression (13) for the derivative of the zero-oscillation energy as a function of the volume into equality (11), we obtain the equation for the determination of pressure in the form

$$P = MRT\gamma_D(V)\left(\frac{3}{8}x_D + D(x_D)\right)\frac{1}{V} + P_y, \quad P_y = -\frac{du_C}{dV}. \quad (14)$$

In order to find a possible dependence of the Grüneisen coefficient for molecular crystals on the volume, we can use the following approach.

The isothermal modulus of compression (modulus of isothermal compressibility) β_T is determined by the expression

$$\frac{1}{\beta_T} = \frac{c_T^2}{V} = -V\left(\frac{\partial P}{\partial V}\right)_T, \tag{15}$$

where the quantity c_T corresponds to the isothermal sonic velocity.

Substituting expression (14) into the right-hand side of equality (15), we arrive at

$$\frac{1}{\beta_T} = -V\frac{\partial}{\partial V}\left\{MRT\gamma_D(V)\left[\frac{3}{8}x_D + D(x_D)\right]\frac{1}{V} + P_y\right\}_T$$

$$= MRT[\gamma_D^2(V) + \gamma_D(V)]\left[\frac{3}{8}x_D + D(x_D)\right]\frac{1}{V} - V\frac{\partial P_y}{\partial V}$$

$$- MRT\gamma_D^2(V)\bar{C}_{v_D}(x_D)\frac{1}{V} - MRT\gamma_D'(V)\left[\frac{3}{8}x_D + D(x_D)\right], \tag{16}$$

where $\gamma_D'(V)$ is the derivative of the Grüneisen coefficient with respect to volume V, and

$$\bar{C}_{v_D}x_D = \left(4D(x_D) - \frac{3x_D}{\exp x_D - 1}\right),$$

$$\frac{\partial x_D}{\partial V} = -\frac{x_D}{V}\gamma_D(V).$$

We now determine the value of the isothermal compressibility as $T \longrightarrow 0$. To this end, we pass to the limit in the last expression:

$$\lim_{T\to 0} MR\rho T[\gamma_D^2(V) + \gamma_D(V)]\frac{3}{8}\gamma_D = \frac{3}{8}\theta_D MR\rho[\gamma_D^2(V) + \gamma_D(V)],$$

$$\lim_{T\to 0} MR\rho T[\gamma_D^2(V) + \gamma_D(V)]D(x_D) = 0,$$

$$\lim_{T\to 0} MR\rho T\gamma_D^2(V)\bar{C}_{v_D}(x_D) = 0,$$

$$\lim_{T\to 0} MRT\gamma_D'(V) \times \frac{3}{8}x_D = \frac{3}{8}MR\theta\gamma_D'(V),$$

$$\lim_{T\to 0} MRT\gamma_D'(V)D(x_D) = 0.$$

Hence, as $T \longrightarrow 0$, the isothermal compressibility is determined by the expression

$$\left(\frac{1}{\beta_T}\right)_{T\to 0} = \frac{3}{8}\theta_D MR\rho[\gamma_D^2(V) + \gamma_D(V)] - \frac{3}{8}MR\theta_D\gamma_D'(V) - V\frac{\partial P_y}{\partial V}. \tag{17}$$

By definition, the isothermal compressibility β_T is associated with the isothermal sonic velocity c_T by formula (15), i.e.,

$$\frac{c_T^2}{V} = \frac{3}{8}\theta_D MR\rho[\gamma_D^2(V) + \gamma_D(V)] - \frac{3}{8}MR\theta_D\gamma_D'(V) - V\frac{\partial P_y}{\partial V}. \tag{18}$$

Assuming further that the sonic velocity is determined only by the elastic properties of a crystal, we obtain the following differential equation analogous to the Bernoulli equation, which allows us to determine the dependence of the Grüneisen coefficient on density:

$$\gamma_D'(V) - \frac{1}{V}\gamma_D^2(V) - \frac{1}{V}\gamma_D(V) = 0.$$

By replacement $z = \frac{1}{\gamma_D(V)}$, we reduce this equation to the linear differential equation

$$z' + \frac{z}{V} = -\frac{1}{V},$$

which is easily integrated. The dependence of the Grüneisen coefficient on density is described by an expression of the form

$$\gamma_D = \frac{V}{C - V}, \tag{19}$$

where the constant C is determined from the condition $\gamma_D(V_0) = \gamma_D^0$. A similar expression for the Grüneisen coefficient was derived on the basis of other concepts by Molodets [3, 6]. As a result, we arrive at the expression

$$\gamma_D = \gamma_D^0\left(\frac{V}{V_0}\right)\left[1 + \gamma_D^0\left(1 - \frac{V}{V_0}\right)\right]^{-1}. \tag{20}$$

In the case of a weak compression, formula (19) transforms into the well-known expression

$$\gamma_D = \gamma_D^0\left(\frac{V}{V_0}\right).$$

Thus, our assumption that at $T = 0$, the isothermal sonic velocity is determined only by the elastic properties of a crystal has made it possible to find the analytical dependence of the Grüneisen coefficient on the specific volume of a solid.

REFERENCES

1. V. N. Zharkov and V. A. Kalinin, *Equations of State at High Pressures and Temperatures* (Nauka, Moscow, 1968; Consultants Bureau, New York, 1971).
2. Yu. M. Kovalev, Fiz. Goreniya i Vzryva **20** (20), 102 (1984).
3. A. M. Molodets, Zh. Éksp. Teor. Fiz. **107**, 824 (1995) [JETP **80**, 467 (1995)].
4. L. Zhirifal'ko, *Statistical Physics of Solids* (Mir, Moscow, 1975) [in Russian].
5. A. I. Kitaĭgorodskiĭ, *Molecular Crystals* (Nauka, Moscow, 1971) [in Russian].
6. A. M. Molodets, Dokl. Akad. Nauk **341**, 753 (1995) [Phys.–Dokl. **40**, 170 (1995)].

Translated by G. Merzon

Doklady Physics, Vol. 50, No. 8, 2005, pp. 397–400. Translated from Doklady Akademii Nauk, Vol. 403, No. 5, 2005, pp. 619–622.

PHYSICS

Generation of Strong Electric Fields by Fluid Flows in Narrow Channels

V. A. Polyanskiĭ and I. L. Pankrat'eva*

Presented by Academician G.G. Chernyĭ February 1, 2005

Received February 4, 2005

In experiments [1] in which flows of weakly conducting hydrocarbon liquids in narrow channels were studied, the luminescence of liquids was observed under certain conditions. In the opinion of the authors of [1], this luminescence was caused by microdischarges in the liquid that acquired an electric potential of several kilovolts while passing through the channel. The luminescence of dielectric liquids of the industrial-oil type due to microdischarges was found experimentally in strong electric fields in the course of developing methods for the electrical cleaning of media from microscopic-scale inclusions [2].

In this paper, we propose a new interpretation of the phenomena that cause the luminescence of dielectric liquids being pumped through narrow channels, and this interpretation is not associated with microdischarges in a medium. Within the framework of electrodynamics, we have theoretically substantiated the possibility of the generation of strong electric fields at phase interfaces for flows of weakly conducting liquids in narrow channels in the presence of surface electrochemical processes. We have also investigated the effect of the parameters of a medium on the field intensity and have proposed a mechanism explaining the observed localization of the luminescence domain. It is shown that, in this case, the electric potential of a liquid moving in a narrow channel does not exceed several tens of millivolts. In the experiments mentioned above, a source of light radiation can be the negative ions that are produced in reactions of electron attachment to molecules of a liquid possessing a high energy of electron affinity. Free electrons appear in the liquid as a result of cold emission from walls, which proceeds in strong induced electric fields.

In the experiments described in [1], industrial oil was pumped through a cylindrical channel with an internal diameter of 1.5×10^{-3} m. The channel was composed of two parts: the input and rest parts were made of fluoroplastic and organic glass, respectively. The parts had smooth internal conjugation with each other. The luminescence of the liquid was observed at the junction of walls made of different materials, the luminescence intensity rapidly dropping as distance from the junction domain increased.

For the theoretical explanation of the phenomenon observed, we analyze the steady-state laminar flow of a liquid with a small admixture of ions of three kinds. The concentrations and charges of the ions are n_m and e_m, respectively ($m = 1, 2, 3$; $e_1 > 0$; and $e_{2,3} < 0$). To simplify our calculation, we assume that the channel is plane, semi-infinite, and has the width h, the channel being at an identical constant electric potential. At the channel input, the medium is considered to be quasi-neutral, with the concentration n_0 of charge carriers originally appearing in the liquid due to the dissociation of admixture molecules of an electrolyte nature ($n_1 = n_2 = n_0$, $n_3 = 0$). The velocity u of the carrier liquid is considered to be given by the Poiseuille formula, insofar as in the absence of external electric fields, a small admixture of charged particles does not affect motion of the medium.

The electrodynamic equations in a two-dimensional Cartesian coordinate system in which the x and y axes are directed along the channel centerline and across the channel, respectively, can be written in the form (see [3])

$$u\frac{\partial n_m}{\partial x} + \frac{\partial}{\partial y}(n_m U_m) = 0, \quad \varepsilon\varepsilon_0\frac{\partial}{\partial y}\left(\frac{\partial F}{\partial y}\right) = -q,$$
$$E = -\frac{\partial F}{\partial y},$$
$$n_m U_m = -D_m\frac{\partial n_m}{\partial x} - \operatorname{sgn}(e_m) b_m n_m \frac{\partial F}{\partial y}, \tag{1}$$
$$q = \sum_m e_m n_m, \quad m = 1, 2, 3.$$

Here, D_m and b_m are the ion diffusivity and mobility; U_m is the ion velocity in the direction normal to the channel

Institute of Mechanics, Moscow State University, Michurinskiĭ pr. 1, Moscow, 119992 Russia

** e-mail: ilpan@imec.msu.ru*

1028-3358/05/5008-0397$26.00

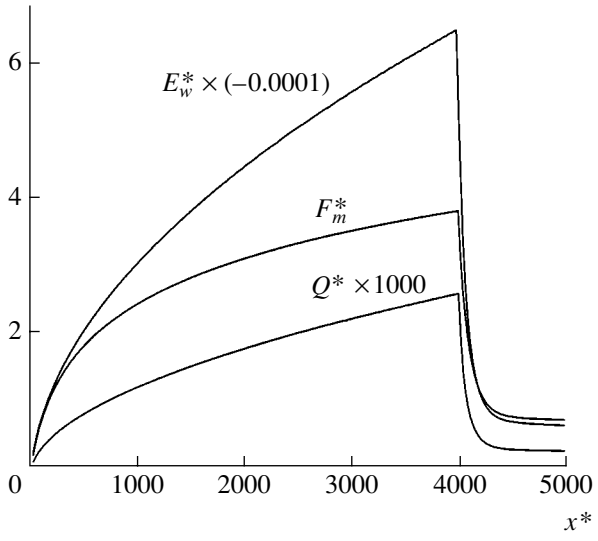

Fig. 1. Distributions for the electric-field strength E_w^* at the channel wall, the maximum value F_m^* of the electric potential in liquid, and the total charge Q^* in a channel cross section along the channel. Injection of ions of kind 3 begins at $x^* = 4000$.

walls; q is the space-charge density, F is the electric potential; E is the transverse component of the electric-field strength; $\varepsilon\varepsilon_0$ is the permittivity.

The formulation of boundary conditions for the concentration of charged components is of crucial importance for the problem under study. In the present paper, we use boundary conditions that are based on the balance of particle flows directed towards channel walls with allowance for the nonequilibrium electrochemical processes of surface ionization and ion recombination [3]. For the sake of certainty, we make the following assumptions. The channel wall is chemically neutral with respect to positive ions, whereas negative ions of kind 2 participate in the surface reactions of recombination and ionization. Negative ions of kind 3, which are absent in the liquid at the channel input, appear as a result of the surface ionization, whose rate is considered to be proportional to the electric-field strength. The formation of ions of kind 3 may be considered to occur by the following process. A strong induced electric field causes cold emission from the channel walls. Insofar as in a liquid the lifetime of emitted free electrons is short, they attach to molecules of the liquid forming negative ions. The majority of hydrocarbon molecules bear a positive affinity to electrons [4]. Therefore, the attachment process can be accompanied by photorecombination luminescence.

With allowance for the aforementioned, relationships at the interface $y = 0$ can be written out in the form (for $y = h$, the conditions are similar)

$$n_1U_1 = 0, \quad n_2U_2 = A_2 - K_2n_2, \quad n_3U_3 = B_3E \quad (B_3 = 0, \quad x < x_0, \quad B_3 > 0, \quad x \geq x_0). \tag{2}$$

The parameters A_2, B_3, and K_2 entering into relationship (2) describe the surface ionization and recombination of ions. These parameters depend on the material of the channel walls and can be different for different segments of the wall. In modeling the discharge process, we suppose that the quantity B_3 is nonzero only on a certain part of the walls, as is written out in (2). This condition takes into account the variation of the channel wall material in [1].

For the electric potential on the walls, we take the condition $F_w = 0$.

Problem (1), (2) is solved numerically. Below, we present the calculation results for a medium of the type of transformer oil with electrolyte additions. These additions make it possible to change within a wide range the conductivity of the medium. To make the equations dimensionless, we have used the characteristic values for the conductivity $\sigma_0 = 10^{-10}$ S m^{-1}, diffusivity $D_0 = 1.34 \times 10^{-9}$ m^2 s^{-1}, velocity $u_0 = 15$ m s^{-1}, electric potential $F_0 = \dfrac{kT}{e}$, electric-field strength $E_0 = \dfrac{F_0}{h}$, total charge in the channel cross section $Q_0 = en_0h$, and the rate of the ion surface recombination $K_{20} = 5 \times 10^{-5}$ m s^{-1} [5]. The concentration n_0 is calculated according to the values of σ_0 and D_0. Low-width channels with a characteristic size $h = 1.5 \times 10^{-3}$ m at $E_0 = 17$ V m^{-1} and $T = 300$ K are analyzed. Below, dimensionless quantities are marked by asterisks.

Figure 1 presents the electric-field strength E_w^* at the wall, the maximum value for the potential of liquid F_m^*, and the total charge Q^* in a channel cross section (obtained by integrating the quantity q along the transverse coordinate) as functions of the longitudinal coordinate x^*. In this calculation, the field-dependent injection of ions of kind 3 is initiated at a distance $x^* = 4000$ from the input. Immediately after the liquid has been injected into the channel, the concentration of negative ions in the vicinity of the wall decreases as a result of the nonequilibrium surface recombination, and a positive space charge begins to be generated in the liquid. The space charge induces a nonuniform electric field directed toward the wall. In the arising field, positive ions that do not react at the surface begin to move from the flow core to the boundary domain. Their concentration rises near the wall, thereby increasing the space charge all the more. In the processes described, along with the electric field, there arise concentration gradients of charged components, which produce diffusion flows of negative ions both towards the wall and from the wall. The diffusion flows of charged components compete with their drift flows under the action of the induced field. The distribution of the dimensionless parameters of the medium in the channel cross section $x^* = 3999$ is shown in Fig. 2. As is seen, the concentra-

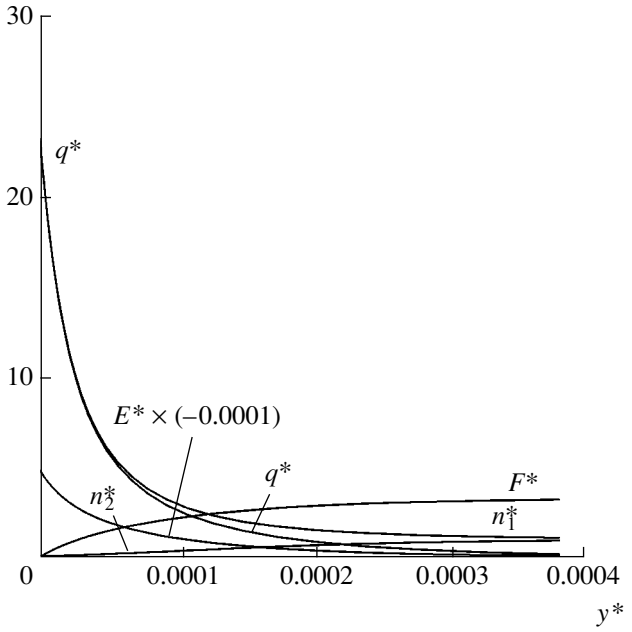

Fig. 2. Distribution of the electric potential F^*, of the electric-field strength E^*, of the space-charge density q^*, and of concentrations of negative n_2^* and positive n_1^* ions in the electrodiffusion boundary layer near the wall $y^* = 0$ for $x^* = 3999$.

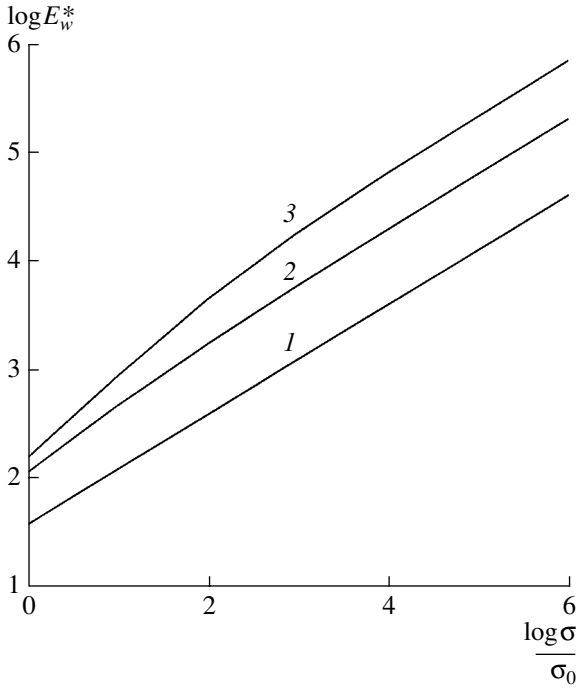

Fig. 3. Electric-field strength E_w^* on the channel wall as a function of the conductivity σ for $x^* = 3999$: (*1*) 10 K_{20}; (*2*) 100 K_{20}; (*3*) 1000 K_{20}.

tion of positive ions n_1^* on the wall exceeds its value at the channel center by a factor of approximately 25. The maximum value of the electric potential F^* of the liquid exceeds the thermal potential by a factor of only 3. The large value of the field at the wall is explained by the fact that the layer in which the charge is concentrated is thin.

The variation of the ion and space-charge concentrations, as well as of the longitudinal convective electric current (stipulated by the space charge), occurs along the channel until a balance of the diffusion flows and ion drift in the transverse direction is established. In this case, the space charge in the cross section and the convective current attain their saturation values and do not further vary along the channel. The tendency to the attainment of saturation is seen even in Fig. 1 in which the rapid rise of electrical parameters in the channel onset is being changed because they are rather slowly approaching the ultimate values. It is worth noting that the field strength at the wall attains a large value and can cause the aforementioned cold emission from the walls. For example, in the cross section in which the injection of ions of kind 3 begins, the true value of the electric field is $E_w = 1102$ kV m^{-1}.

After the injection (whose intensity is time-dependent) has begun, negative ions of kind 3 compensate at a short distance the positive space charge near the wall, the field rapidly drops, the injection of ions of kind 3 decreases, and the electrical parameters pass to a new equilibrium state at a considerably lower level.

The numerical experiments allow us to determine two basic parameters that strongly affect the field strength at the wall. We refer here to the conductivity of liquid and the rate of surface recombination for ions of kind 2. The calculation results are demonstrated in Fig. 3. There, bilogarithmic dependences for the field at the wall are presented as functions of the surface recombination rate for ions of kind 2 (curves *1*, *2*, and *3* correspond to 10 K_{20}, 100 K_{20}, and 1000 K_{20}, respectively). The bilogarithmic dependences of the field at the wall as a function of the conductivity are close to linear ones. This is especially clearly seen for curve *1*, for which the field at the wall can be written out as $E_w^* \approx \left(\frac{\sigma}{\sigma_0}\right)^{0.5}$. We should note that, varying (in correspondence with Fig. 3) parameters of the medium in a physical experiment, we can use the variation of luminescence to obtain information on the adequacy of the theoretical model in relation to the actual phenomenon.

Thus, within the framework of the electrodynamic model of a medium, we have shown that the separation of charges in a thin electrodiffusion boundary layer at the phase interface is accompanied by the generation of strong electric fields. These fields are capable of causing cold emission from the channel wall and the luminescence of a fluid moving through a narrow channel. This phenomenon is determined by the attachment of

electrons to molecules that bear a positive electron affinity. The form of the radiation spectrum obtained in [1] confirms that the processes occurring near the interface [6] have their origin in photorecombination.

ACKNOWLEDGMENTS

We are grateful to A.A. Monakhov for fruitful discussions.

This work was supported by the Russian Foundation for Basic Research, project no. 04-01-00078.

REFERENCES

1. S. Ya. Gertsenshteĭn, A. A. Monakhov, D. S. Baranov, *et al.*, in *Theses of Reports of XII School–Seminar. Modern Problems of Aerohydrodynamics* (Moscow, 2004), pp. 15–16 [in Russian].
2. M. G. Granovskiĭ, I. S. Lavrov, and O. V. Smirnov, *Electrotreatment of Liquids* (Khimiya, Leningrad, 1976) [in Russian].
3. V. V. Gogosov, K. V. Polyansky, V. A. Polyansky, *et al.*, J. Electrost. **34**, 245 (1995).
4. V. I. Vedeneev, L. V. Gurvich, V. N. Kondrat'ev, *et al.*, *Break Energies of Chemical Bonds. Ionization Potentials and Electron Affinity* (Akad. Nauk SSSR, Moscow, 1962) [in Russian].
5. T. Pillat, E. Moreau, and G. Touchard, J. Electrost. **53**, 172 (2001).
6. H. S. W. Massey, *Negative Ions* (Cambridge Univ. Press, Cambridge, 1976; Mir, Moscow, 1979).

Translated by G. Merzon

Doklady Physics, Vol. 50, No. 8, 2005, pp. 401–404. Translated from Doklady Akademii Nauk, Vol. 403, No. 5, 2005, pp. 623–626.

PHYSICS

Atomic Models of the Nucleation of Dislocations and Mechanical Twinning in fcc Crystals

A. N. Tyumentsev, I. Yu. Litovchenko, Yu. P. Pinzhin, and N. V. Shevchenko

Presented by Academician V.E. Panin March 21, 2005

Received March 21, 2005

In [1, 2], in order to explain the laws of formation of deformation localization bands in austenite steels, a new mechanism of the deformation and reorientation of a crystal lattice was proposed. This is the mechanism of direct plus inverse (through alternative systems) of martensitic transformations in fields of high local stresses. In our opinion, this mechanism is a clear illustration and represents the first atomic model of the nonequilibrium local structure transformations that were introduced in the concept of physical mesomechanics [3, 4] as carriers of plastic deformations in stress-concentrator zones.

In this work, using the mechanism of reversible martensitic transformations and martensitic transformation theory [5] based on the concept of the cooperative thermal vibrations of extended two-dimensional objects (close packed planes) in crystals, we develop atomic models of the formation (nucleation) of dislocations and deformation twins in fcc crystals.

MODELS OF NUCLEATION OF PARTIAL (SHOCKLEY) DISLOCATION AND TOTAL DISLOCATION

According to [5], atomic rearrangements in the process of bcc ⟶ fcc and bcc ⟶ hcp transformations are combinations of shear and contraction (Bein-type) deformation modes. The shear component appears due to the freezing of cooperative thermal vibrations of atoms of close packed planes (such as {110}) of the bcc phase in directions such as ⟨110⟩. It is equal to the double amplitude of these vibrations and is limited by the free paths (up to collisions with neighboring atoms) of atoms in the bcc lattice. The direction and value of contraction displacements are determined by the tendency of atoms to pack closer and to occupy energetically favorable states in the structure of a new martensitic phase. If such rearrangements involve one family of planes and the mutual displacements between pairs of neighboring planes are accumulated from plane to plane, a bcc ⟶ fcc transformation is observed. If mutual displacements are compensated in each sequential interplanar interval, bcc ⟶ hcp transformations occur.

The concept of the model presented below is to attribute the nucleation of the dislocation displacement with the load-induced shear component of the local fcc ⟶ bcc ⟶ fcc transformation. The scheme of such a transformation that is localized in two adjacent slip planes of the fcc lattice (atoms of these planes are shown by open symbols) is shown in Fig. 1. Let us consider a variant of the local stress field with a large shear component τ acting in the (111) slip plane in the direction of the Burgers vector of the Shockley partial dislocation $\frac{a}{6}[1\bar{2}1]$ (see $\tau_{[1\bar{2}1]}$ in Fig. 1a). Under the conditions of constrained deformation, the responses to this component are large diagonal components of the stress tensor (σ_{ii} in Fig. 1a), i.e., compression stress in the $[1\bar{2}1]$ direction and tensile stresses in the $[\bar{1}01]$ and [111] directions that are perpendicular to the former one.

The geometry of these stresses is such that the directions of the corresponding tensile–compression deformations (ε_{ii} in Fig. 1b) are similar to those for contraction displacements of atoms in the process of the fcc ⟶ bcc transformation. The atomic configuration after such displacements localized in two neighboring slip planes is shown in Fig. 1b. The values of these displacements, as well as those of the tensile–compression deformation components, are not strictly determined for two reasons. First, the intermediate bcc phase is absent in the equilibrium diagram of state for fcc metals with a high packing-defect energy and is virtual in this case; i.e., it exists only in the process of deformation in the field of high local stresses. Second, the parameters of this phase can depend strongly on these stresses. The ε_{ii} values obtained under the assumption that the atomic size does not change in the transformation process are indicated in Fig. 1b.

Institute of Strength Physics and Materials Science, Siberian Division, Russian Academy of Sciences, Akademicheskiĭ pr. 2/1, Tomsk, 634021 Russia
e-mail: tyuments@phys.tsu.ru

1028-3358/05/5008-0401$26.00

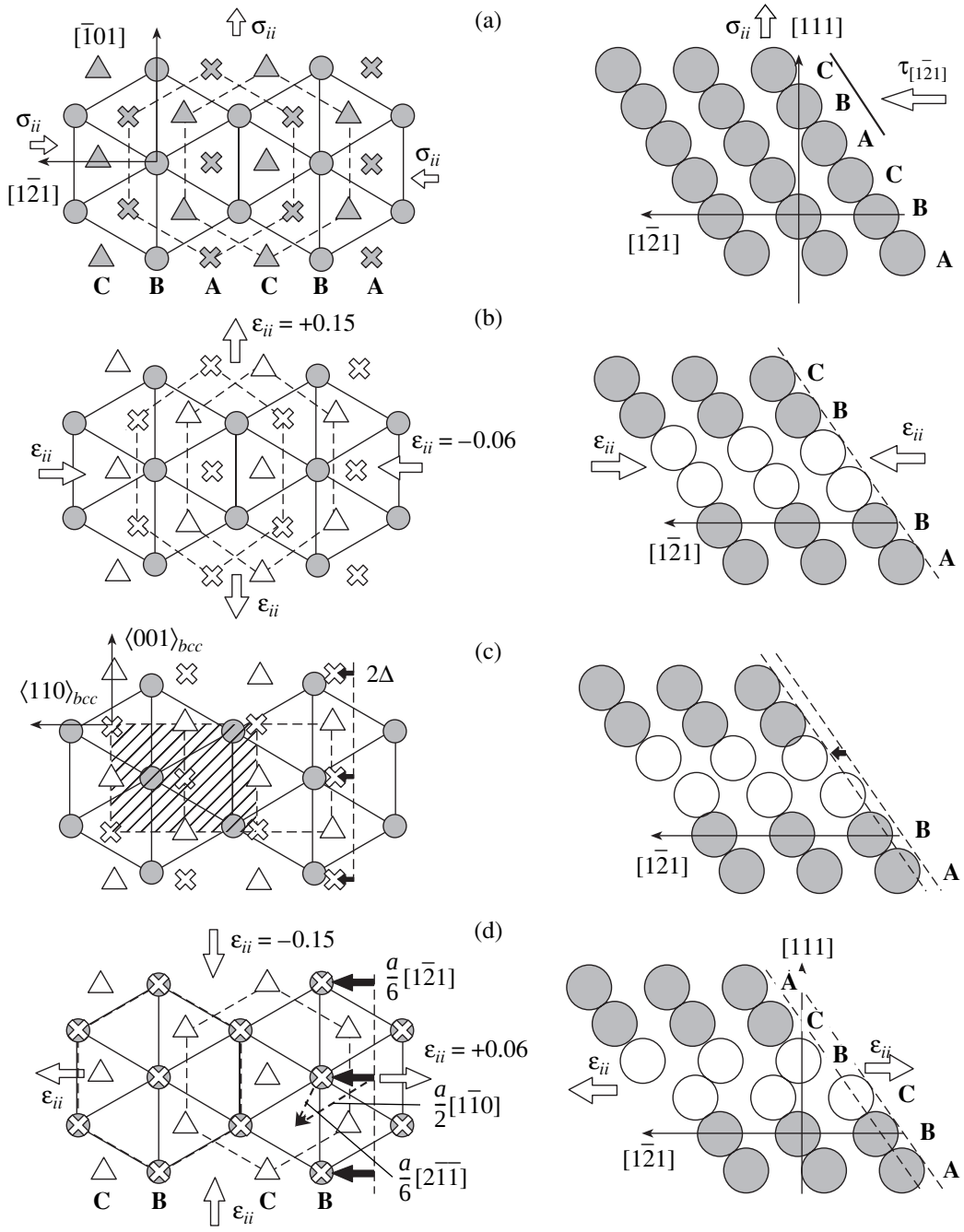

Fig. 1. Atomic configurations at various stages of the direct plus inverse (fcc–bcc–fcc) martensitic transformation that is localized in two adjacent slip planes and leads to the formation of Shockley partial dislocation in (left panels) a section parallel to the (111) slip plane and (right panels) a section parallel to the $(10\bar{1})$ plane that is perpendicular to the slip plane and is parallel to the Burgers vector of the dislocation after (b) the contraction plus (c) shear deformation modes of the direct transformation and (d) the direct and inverse transformations.

According to [5], if the contraction displacements under the action of the shear stress component in the $[1\bar{2}1]$ direction of the fcc phase are accompanied by the mutual displacement of planes in this direction by the double amplitude of the cooperative thermal vibrations of atoms in the bcc lattice (2Δ in Fig. 1c), the resulting atomic configuration consists of two close packed planes of the bcc lattice. A cell with an atomic configuration characteristic of such a pair of planes is shaded in Fig. 1c.

This configuration is nonequilibrium with a strong thermodynamic stimulus of the inverse bcc $\longrightarrow$ fcc transformation. In this case, only two variants of such a transformation are possible: first, strictly backward

with reversal of the signs of both contraction and shear deformation modes and, second, with the shear component in the direction of the displacement of the direct deformation. The first variant leads to the initial crystal (Fig. 1a). However, the existence of the shear stress components and the necessity of its relaxation stimulate the realization of the second variant of the inverse transformation. In the process of such a transformation (shift by 2Δ in the $[1\bar{2}1]$ direction plus contraction shifts directed towards the formation of the close packed structure of the fcc phase), the atoms of the transformation plane **C** that are indicated by triangles occupy close packing sites in the fcc lattice of the lower part of the crystal, and the atoms of the transformation plane **A** (shown by crosses) are shifted along with the upper part of the crystal to the sites of the close packing over the atoms of the planes **B** (see Fig. 1d). As a result, the shift by the Burgers vector of the Shockley partial dislocation ($\mathbf{b} = \frac{a}{6}[1\bar{2}1]$) occurs in the (111) plane with the formation of the subtraction packing defect (**ABCABC**… ⟶ **ABCBCA**…) in this plane.

If the local stress is such that the shear stress component comparative with $\tau_{[1\bar{2}1]}$ acts also in the $[2\bar{1}\bar{1}]$ direction (see Fig. 1d) or the $[\bar{1}\bar{1}2]$ direction, the formation of Shockley partial dislocations with the Burgers vector $\frac{a}{6}[2\bar{1}\bar{1}]$ or $\frac{a}{6}[\bar{1}\bar{1}2]$ is possible through a mechanism similar to that shown in Figs. 1a–1d. Moving in the same slip plane, these dislocations recover the packing of the fcc phase (**ABCBCA**… ⟶ **ABCABC**…) and, together with the first dislocation, make shifts by the Burgers vector $\frac{a}{2}[1\bar{1}0]$ (Fig. 1d) or $\frac{a}{2}[0\bar{1}1]$ of the total dislocations.

The variants of fcc ⟶ bcc ⟶ fcc transformations that are shown in Fig. 1 give rise to the formation (nucleation) of partial (Shockley) dislocation or total dislocation. If local martensitic transformations begin at the intercrystalline boundary and propagate in the transformation plane into the grain bulk under the action of the shear component τ, dislocations originate at the grain boundary. When these transformations occur in the grain bulk, loops of partial or total dislocations are formed.

FORMATION OF DEFORMATION TWINS

When local shear stresses reduced to the shear directions of driven dislocations ($\tau_{[2\bar{1}\bar{1}]}$ or $\tau_{[\bar{1}\bar{1}2]}$) are much lower than $\tau_{[1\bar{2}1]}$ and are insufficient for the nucleation of these dislocations, the relaxation of the local stress field can proceed through the nucleation and motion of partial dislocations $\frac{a}{6}[1\bar{2}1]$ in the slip planes parallel to the slip plane of the first dislocation. If each sequential dislocation slips in the neighboring plane, a deformation microtwin nucleates and grows.

We discussed above the variants of direct plus inverse martensitic transformations localized in two adjacent slip planes. In this case, a dislocation arises as a linear defect bounding the 2D transformation region and is in essence the front of this transformation. At the same time, the variant of this transformation that occurs simultaneously in several (more than two) neighboring slip planes or the motion of the transformation front in the third direction perpendicular to the slip plane is not excluded. In this case, the front of the local martensitic transformation is a 2D defect bounding a 3D region, where shifts by the Burgers vector of the Shockley partial dislocation occur in each plane; i.e., it is the region of a twinned crystal. We note that such a twinning mechanism, which is based on the motion of the high-angle boundary that produces a pair of coherent twinning boundaries after it, was discovered recently [6] in the plastic deformation of nanocrystalline aluminum.

DISCUSSION OF THE RESULTS

According to [7], the motion of the total dislocation $\frac{a}{2}\langle 110\rangle$ in the fcc crystal through the sequential motion of a pair of Shockley partial dislocations may be favorable, because the distortion of the crystal lattice is much lower than the value in the direct shift by the Burgers vector of the direct dislocation. In the atomic model presented in this paper, this distortion is reduced to the distortion of the local fcc ⟶ bcc phase transition, and the shear direction is the direction of the cooperative thermal vibrations of the atoms of close packed planes in the bcc phase. In this case, the shift by the Burgers vector of the Shockley partial dislocation is a result of the cooperative shifts of atoms by distances that do not exceed their free paths (up to collision with neighboring atoms) in the intermediate martensitic phase.

In this case, the energy barrier of the nucleation of a partial dislocation necessarily includes the energy of the local fcc ⟶ bcc transformation. Therefore, the phase instability of the crystal in the field of high local stresses is an important factor underlying the above atomic mechanisms of the formation of partial dislocations and deformation microtwins. The most favorable conditions for the formation of such stresses are evidently high deforming stresses and low efficiency of their relaxation through the standard mechanisms of generation and motion of dislocations, when, in particular, the critical work stress of a Frank–Read source becomes higher than the stress of the local martensitic transformation leading to the formation of a local dislocation or a deformation microtwin.

The above models are of considerable interest in the physical mesomechanics of the surface layers of solids.

According to the concepts developed in this field [8], a surface layer is treated as a special state of matter that is characterized by a specific crystalline structure with several atomic configurations, including those that are not inherent in the crystalline structure of the material bulk, increased concentration of vacancies, softening of phonon modes, etc. As was shown in [8], these properties give rise to the development of specific deformation mechanisms at micro-, meso-, and macroscales in the surface layers of a loaded material. The initial displacements and dislocations associated with them nucleate primarily on the surface. However, the mechanism of this nucleation is not yet known, as was mentioned in [8]. We believe that the mechanism of the direct plus inverse martensitic transformation localized in two neighboring slip planes may serve as such a mechanism in fcc crystals. In this mechanism, the role of the free surface is not only in the presence of stress concentrators but also in the reduction of the phase stability of the initial fcc phase. This reduction is reliably corroborated by the aforementioned softening of phonon modes and by the existence of atomic configurations whose crystalline structure is not inherent in this phase. Local regions of such configurations can be potential nuclei of local martensitic transformations as dislocation nucleation mechanisms.

We emphasize that the above reversible martensitic transformations in materials with relatively high phase stability develop in fields of high local stresses. In this case, direct martensitic transformations result from the phase instability of the crystal in stress fields, and they provide a pathway for the plastic relaxation of these fields. The choice of the system of the inverse transformation is determined both by the character of the local stress field and by the necessity of the plastic deformation of transformed volumes for the relaxation of this stress field.

Since the Bein-type transformation deformation (ε_{ii} in Fig. 1) is an important deformation mode in this process, its carriers are necessarily volume structures. These may be microvolumes of unstable (stables in stress fields?) martensitic phases or of nonequilibrium phase-structure states that are superpositions of two structures, when the interstitial space of the initial crystal contains new allowed states—sites of the martensitic phase. The plastic deformation and reorientation of the crystal lattice occur by means of the motion of atoms through these states. In contrast to, e.g., dislocations, such carriers exist only in the process of deformation in fields of high local stresses.

In conclusion, we emphasize that, if change in the inverse-transformation system in the process of the fcc $\longrightarrow$ bcc $\longrightarrow$ fcc transformation is associated with change in the transformation plane, this mechanism explains the features of the reorientation of the crystal lattice in the deformation localization bands formed when rolling austenitic steels [1, 2]. The properties of formation of bands of the localization and deformation twins in planes with various indices ({112}, {113}, and {225}) in titanium nickelide were described in [9, 10] in the framework of the model of the direct plus inverse B2 $\longrightarrow$ B19 $\longrightarrow$ B2 transformation.

ACKNOWLEDGMENTS

We are grateful to Prof. A.D. Korotaev for stimulating discussions concerning the results. This work was supported in part by the Basic Research and Higher Education Program, the Ministry of Education of the Russian Federation, the U.S. Civilian Research and Development Foundation (grant no. BRHE 016-02), and by the Russian Foundation for Basic Research (project nos. 03-03-33079 and 05-03-98003).

REFERENCES

1. A. N. Tyumentsev, I. Yu. Litovchenko, Yu. P. Pinzhin, *et al.*, Fiz. Met. Metalloved. **95** (2), 86 (2003) [Phys. Met. Metallogr. **95** (2), 186 (2003)].
2. A. N. Tyumentsev, A. D. Korotaev, Yu. P. Pinzhin, *et al.*, Izv. Vyssh. Uchebn. Zaved., Fiz., No. 8, 28 (2004).
3. V. E. Panin, in *Physical Mesomechanics and Computer Simulation of Materials* (Nauka, Novosibirsk, 1995), Vol. 1, pp. 7–49 [in Russian].
4. V. E. Panin, Fiz. Mezomekh. **1** (1), 5 (1998).
5. F. A. Kassan-Ogly, V. E. Naĭsh, and I. V. Sagaradze, Fiz. Met. Metalloved. **65** (3), 481 (1988).
6. X. Z. Liao, F. Zhou, E. J. Lavernia, *et al.*, Appl. Phys. Lett. **83** (24), 5062 (2003).
7. J. P. Hirth and J. Lothe, *Theory of Dislocations* (McGraw-Hill, New York, 1967; Atomizdat, Moscow, 1972).
8. V. E. Panin, Fiz. Mezomekh. **2** (6), 5 (1999).
9. A. N. Tyumentsev, N. S. Surikova, I. Yu. Litovchenko, *et al.*, Fiz. Met. Metalloved. **95** (1), 97 (2003).
10. A. N. Tyumentsev, N. S. Surikova, I. Yu. Litovchenko, *et al.*, Acta Mater. **52**, 2067 (2004).

Translated by R. Tyapaev

Doklady Physics, Vol. 50, No. 8, 2005, pp. 405–408. Translated from Doklady Akademii Nauk, Vol. 403, No. 4, 2005, pp. 478–481.

TECHNICAL PHYSICS

Propagation of Detonation Waves along a Tubular Bubble Cluster in Liquid

Academician R. I. Nigmatulin*, V. Sh. Shagapov, I. K. Gimaltdinov**, and A. R. Bayazitova****

Received March 24, 2005

In this paper, we consider the dynamics of deformation-wave propagation along a tubular volume in a bubble liquid containing a chemically-active gas mixture. Such a bubble cluster is shown to serve as a waveguide capable of transmitting pulsed signals in the form of detonation solitons. In order to prevent the stall of detonation solitons due to the acoustic-wave emission into the bulk of liquid surrounding the waveguide, its radius must exceed a certain critical value that depends on the radii of bubbles, as well as on their volume content and characteristics of the explosive gas mixture.

Let the tubular volume of radius R_0 be filled with a homogeneous bubble medium containing a combustible gas mixture (e.g., mixture of $C_2H_2 + 2.5O_2$). There is a pure liquid around the tubular volume (i.e., for $r_0 > R_0$, see Fig. 1). At the instant of time $t = 0$, a piston begins to act in order to initiate the detonation at the boundary of the tubular volume ($z_0 = 0$, $0 < r_0 < R_0$). The rest part of the boundary ($z_0 = 0$, $r_0 > R_0$) remains free. Below, the action of the gravity force is ignored.

To describe the further evolution of the wave in this system, we take the following equations for the bubble liquid [1, 2], which are written out in the two-dimensional radial-symmetric approximation and have the following form in Lagrangian variables:

$$\frac{\partial \upsilon_z}{\partial t} = \frac{r}{r_0}\frac{1}{J\rho}\left(\frac{\partial p_l}{\partial r_0}\frac{\partial r}{\partial z_0} - \frac{\partial p_l}{\partial z_0}\frac{\partial r}{\partial r_0}\right), \quad \frac{\partial z}{\partial t} = \upsilon_z,$$

$$\frac{\partial \upsilon_r}{\partial t} = \frac{r}{r_0}\frac{1}{J\rho}\left(\frac{\partial p_l}{\partial r_0}\frac{\partial r}{\partial z_0} - \frac{\partial p_l}{\partial z_0}\frac{\partial r}{\partial r_0}\right), \quad \frac{\partial r}{\partial t} = \upsilon_r,$$

$$\frac{\partial p_g}{\partial t} = -\frac{3\gamma p_g}{a}w - \frac{3(\gamma-1)}{a}q,$$

$$\frac{\partial a}{\partial t} = w = w_R + w_A,$$

$$\frac{\partial w_R}{\partial t} = \left(\frac{p_g - p_l}{\rho_l^0} - \frac{3}{2}w_R^2 - 4\nu_l\frac{w_R}{a}\right)\frac{1}{a}, \quad w_A = \frac{p_g - p_l}{\rho_l^0 C_l \alpha_g^{1/3}},$$

$$\frac{\partial \alpha_g}{\partial t} = 3\frac{\alpha_g w}{a} - \frac{\alpha_g}{J}\frac{\partial J}{\partial t},$$

$$\frac{\partial p_l}{\partial t} = \frac{C_l^2\rho_l^0}{1-\alpha_{g0}}\left(\frac{3\alpha_g w}{a} - \frac{\partial J}{\partial t}\left(\frac{\rho_{l0}}{\rho_l^0 J^2} + \frac{\alpha_g}{J}\right)\right), \tag{1}$$

$$q = \mathrm{Nu}\lambda_g\frac{T_g - T_0}{2a}, \quad \frac{T_g}{T_0} = \frac{p_g}{p_0}\left(\frac{a}{a_0}\right)^3,$$

$$\mathrm{Nu} = \sqrt{\mathrm{Pe}}, \quad \mathrm{Pe} \geq 100, \quad \mathrm{Nu} = 10, \quad \mathrm{Pe} < 100,$$

$$\mathrm{Pe} = 12(\gamma-1)\frac{T_0}{|T_g - T_0|}\frac{a|w|}{\kappa_g}, \quad \kappa_g = \frac{\lambda_g}{c_g\rho_g},$$

$$\alpha_l + \alpha_g = 1, \quad \rho_i = \rho_i^0\alpha_i,$$

$$\alpha_g = \frac{4}{3}\pi n a^3, \quad \rho = \rho_g + \rho_l,$$

$$J = \frac{r}{r_0}\left(\frac{\partial z}{\partial z_0}\frac{\partial r}{\partial r_0} - \frac{\partial z}{\partial r_0}\frac{\partial r}{\partial z_0}\right),$$

$$\frac{\partial J}{\partial t} = \frac{\upsilon_r J}{r} + \frac{r}{r_0}\left(\frac{\partial \upsilon_z}{\partial z_0}\frac{\partial r}{\partial r_0} + \frac{\partial z}{\partial z_0}\frac{\partial \upsilon_r}{\partial r_0} - \frac{\partial \upsilon_z}{\partial r_0}\frac{\partial r}{\partial z_0} - \frac{\partial z}{\partial r_0}\frac{\partial \upsilon_r}{\partial z_0}\right).$$

The subscripts $i = l, g$ mark the parameters of the liquid and gas phases, and the subscript 0 corresponds to the initial state. Here, p_i are phase pressures; ρ_i^0 are the true phase densities; α_i are the volume phase contents; n is the number of bubbles per unit volume; a is the bubble radius; w is the radial velocity of bubbles; ν_l is the kinematic viscosity of the carrier phase; C_l is the sonic velocity in liquid; T_0 = const is temperature of liquid;

* *Institute of Mechanics, Ufa Research Center, Russian Academy of Sciences, ul. Karla Marksa 6, Ufa-center, Bashkortostan, 450000 Russia*

** *Sterlitamak State Pedagogical Academy, pr. Lenina 37, Sterlitamak, Bashkortostan, 453103 Russia*

e-mail: iljas_g@mail.ru; Stlina@rambler.ru

1028-3358/05/5008-0405$26.00

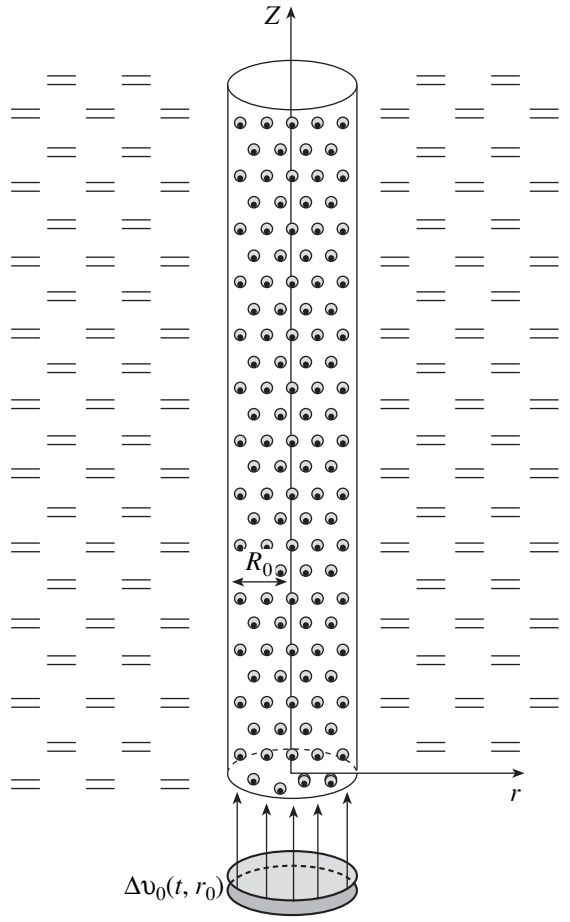

Fig. 1. Illustration of the problem under study.

q is the heat-exchange intensity; γ is the adiabatic index for gas; λ_g is the thermal conductivity; Nu and Pe are the Nusselt and Pecklet numbers, respectively; z_0 and r_0 are the Lagrangian variables (for them, we take the initial cylindrical coordinates); and J is the Jacobian of mapping from Lagrangian to Eulerian variables. The velocities υ_r and υ_z correspond to motion over coordinates r and z.

Henceforth, we assume that, in the initial state ($t = 0$), the system under consideration is at rest. Then, we may write out the following initial conditions:

$$p_l = p_0, \quad \upsilon_r = \upsilon_z = 0, \quad \rho = \rho_0;$$

$$\alpha_g = \alpha_{g0}, \quad \rho_0 = \rho_{l0}^0(1 - \alpha_{g0}),$$

$$p_g = p_0, \quad a = a_0, \quad w = 0 \quad (0 < r < R_0);$$

$$a_{g0} = 0, \quad \rho_0 = \rho_{l0}^0 \quad (r > R_0) \text{ for } t = 0, \quad z_0 > 0.$$

We specify the initiating pulse at the boundary of the tubular bubble volume ($z_0 = 0$, $0 < r_0 < R_0$) in the form of a bell-shaped time law for the velocity of a rigid striker, whereas the rest boundary ($z_0 = 0$, $R_0 < r_0 < \infty$) is free. We can write out the corresponding boundary conditions as

$$\upsilon_0(t, r_0) = \begin{cases} \Delta\upsilon_0 \exp\left(-\left(\dfrac{t - t_*/2}{t_*/6}\right)^2\right), & 0 < t < t_*, \\ 0, & t > t_* \end{cases}$$

for $z_0 = 0$, $0 < r_0 < R_0$ and $p_l = p_0$ for $z_0 = 0$, $R_0 < r_0 < \infty$, where $\Delta\upsilon_0$ is the velocity amplitude and t_* is the characteristic duration of a pulse.

The impermeability condition ($\upsilon_r = 0$) is specified at the symmetry axis ($r_0 = 0$). At the cylindrical boundary ($r_0 = R_0$) of the calculation region, the reflection-free conditions [3] are posed in the form of the impedance relation $\Delta p_l = \Delta\upsilon_r \rho_l C_l$, where Δp_l and $\Delta\upsilon_r$ are current perturbation values for pressure and radial velocity at the calculation-region boundaries of the Lagrangian system.

We allow for the inflammation of bubbles in accordance with the instantaneous scheme. According to this scheme, after the gas temperature in bubbles has attained a certain value T_*, the temperature instantaneously increases by the value ΔT, which corresponds to the caloric power of the combustible-gas mixture in bubbles.

Figure 2a exhibits plots for pressure in liquid and gas temperature in bubbles, which illustrate the dynamics of the detonation wave along a cylindrical bubble cluster of radius $R_0 = 0.05$ m. For parameters that determine both the system and an initiating signal, the following values are taken: $p_0 = 0.1$ MPa; $\rho_{l0}^0 = 1130$ kg m^{-3}; $C_l = 1700$ m s^{-1}; $\nu_l = 6 \times 10^{-6}$ m^2 s^{-1}; $\chi_l = 4.65 \times 10^{-7}$ m^2 s^{-1}; $T_0 = 293$ K; $\gamma = 1.35$; $\rho_{g0}^0 = 1.3$ kg m^{-3}; $c_g = 1.14 \times 10^3$ J (kg K)$^{-1}$; $T_* = 1000$ K; $\Delta T = 3000$ K; $\alpha_{g0} = 0.01$; $a_0 = 10^{-3}$ m; $\Delta\upsilon_0 = 10.5$ m s^{-1}; and $t_* = 0.1$ ms. Here, as in other figures, the pressure distributions are presented for the entire axial cross section ($-R_{c0} < r_0 < R_{c0}$).

Under the action of the boundary pulse, the temperature inside bubbles in the zone near the piston attains the value T_*, and a self-maintaining detonation wave arises. In the upper part of Fig. 2a, it is shown that the detonation wave propagates along the cylindrical bubble cluster and is accompanied by a wave packet in the ambient liquid, which is caused by acoustic radiation from the detonation-wave zone. In the lower part of Fig. 2a, the pressure distributions Δp_l ($\Delta p_l = p_l - p_0$) along the cluster axial line (solid curves) and at a certain distance ($r_0 = 0.1$ m) from the axial line (dashed curve) in the liquid are presented. As is seen, the background wave in liquid, which accompanies the detonation wave, also has the shape of a spread soliton with a

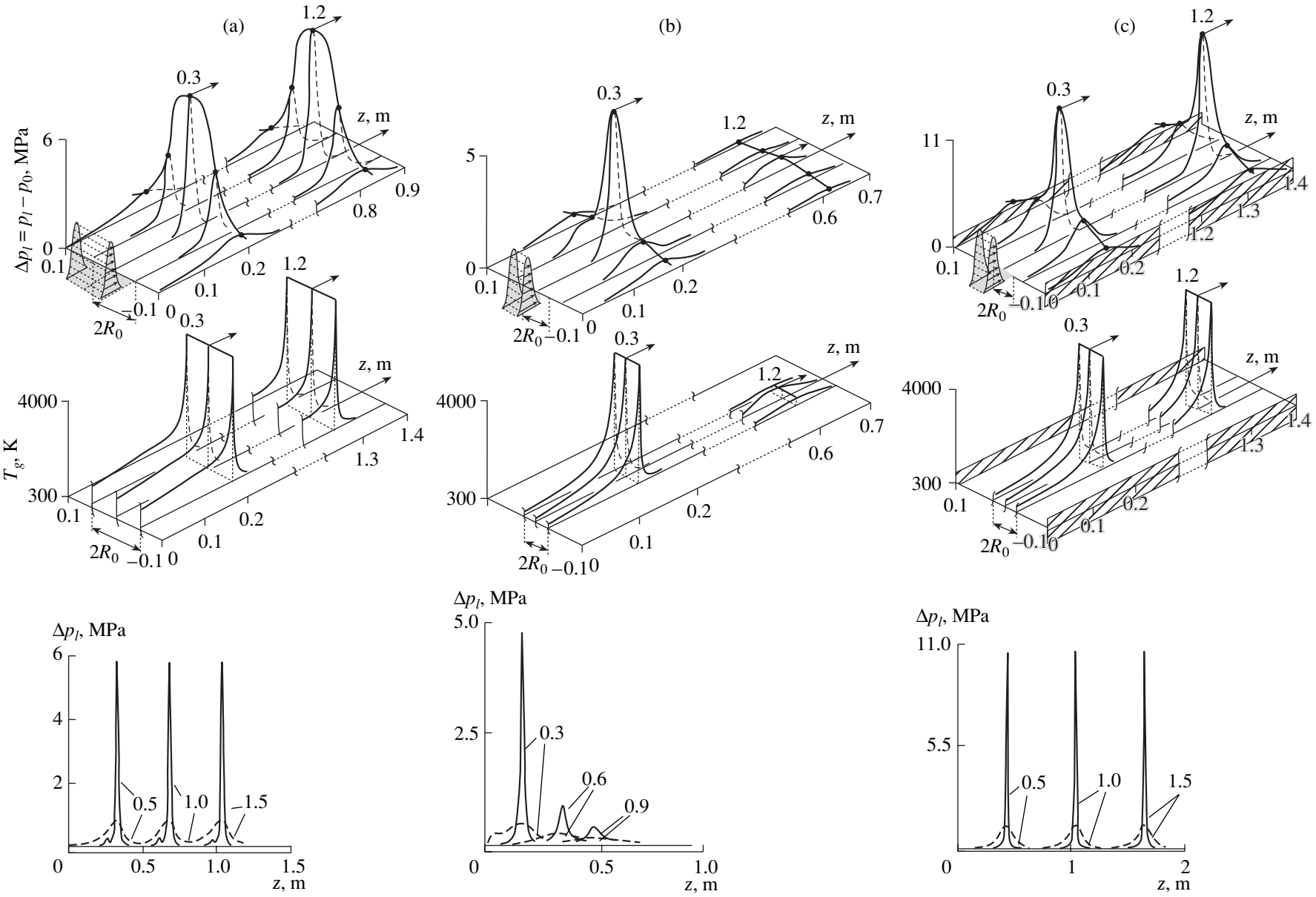

Fig. 2. Propagation of a detonation wave in the case of (a) R_0 = 5 cm; (b) R_0 = 2.5 cm; (c) the same as in Fig. 2b but the boundary $r = R_{C0}$ = 10 cm is the rigid wall. Numerical marks at the curves correspond to instants of time t expressed in milliseconds. Solid and dashed curves correspond to the pressure distributions on the axis and at a distance r = 10 cm.

considerably lesser amplitude compared to that of the detonation signal.

Figure 2b illustrates the results of our numerical experiment for the same parameters of the bubble system and the initiating signal as in Fig. 2a but with a lesser radius (R_0 = 0.025 m) of the bubble cluster. It is seen that, against the background of the detonation wave at the instant of time t = 0.3 ms, pressure waves after the stall has occurred at the instant of time 1.2 ms are virtually unnoticeable. Under the action of the piston, the gas temperature in cluster bubbles near the piston boundary attains the value T_*, and the detonation is thereby initiated. However, the arisen detonation center is not further capable of additionally compressing bubbles located in the foreground to increase their temperature up to the temperature T_*, and therefore, the detonation stalls. The basic reason for the stall is an increase (with a decrease in the cluster radius) in the specific lateral bubble-cluster boundary through which the acoustic radiation propagates into the ambient liquid.

To illustrate the role of the acoustic-radiation emission into the ambient liquid, we present in Fig. 2c the calculation results for the case in which a bubble cluster of radius R_0 = 0.025 m is placed into a cylindrical channel of radius R_{C0} = 0.1 m with rigid walls. In this situation, the condition $\upsilon_r = 0$ for $r_0 = R_{C0}$ is specified on the surface of the cylindrical channel. As is seen, in this case, in which the acoustic-radiation emission into the ambient liquid is screened by the rigid wall, the stable propagation of a self-maintained detonation soliton is observed. In the lower part of Fig. 2c, pressure distributions along the axial line and at the distance of r_0 = 0.1 m are presented for a number of time instants. In this case, the amplitudes of both the detonation soliton and the accompanying wave that propagates through the liquid and is located between the cluster and channel walls exceed, approximately by a factor of two, the values obtained for reflection-free conditions at the boundary of radius R_{C0}, although, in this case, the bubble-cluster radius is smaller by a factor of two (R_0 = 0.025 m) than in the case shown in Fig. 2a (R_0 = 0.05 m).

When we employ waveguides of such a type, a danger arises to the survival of the underwater fauna, because, as is seen from Fig. 2a, the acoustic wave in pure liquid, which accompanies the detonation wave, has an amplitude of ~8 atm at a distance of 10 cm from the axis of the bubble cluster. However, as the calculations have shown, even at a distance on the order of 1 or 2 m, the amplitudes of the acoustic wave become smaller than $\Delta p_l = 10^4$ and 10^3 Pa, respectively. This is associated with the fact that such a strong damping is determined not only by the spherical scattering of the acoustic wave of the detonation soliton into the volume of the ambient bulk of liquid but also by the unloading coming from the waveguide. Indeed, after the detonation wave has passed, the waveguide surface plays the role of a free surface for perturbations propagating in the liquid surrounding the waveguide.

REFERENCES

1. R. I. Nigmatulin, *Dynamics of Multiphase Mediums* (Nauka, Moscow, 1987), Vol. 1 [in Russian].
2. R. I. Nigmatulin, V. Sh. Shagapov, and N. K. Vakhitova, Dokl. Akad. Nauk SSSR **304**, 1077 (1989) [Sov. Phys. Dokl. **34**, 98 (1989)].
3. M. A. Il'gamov and A. N. Gil'manov, *Nonreflecting Conditions at Boundaries of the Calculation Region* (Fizmatlit, Moscow, 2003) [in Russian].

Translated by G. Merzon

Doklady Physics, Vol. 50, No. 8, 2005, pp. 409–413. Translated from Doklady Akademii Nauk, Vol. 403, No. 6, 2005, pp. 756–760.

TECHNICAL PHYSICS

Structural Mechanisms of Plastic Strain in Bulk-Amorphous Metallic Alloys

Academician Yu. K. Kovneristyĭ* and V. A. Pozdnyakov**

Received April 8, 2005

INTRODUCTION

In this paper, we perform a theoretical analysis of the structural mechanisms of low-temperature plastic strain for bulk-amorphous metallic alloys. We have studied the mechanisms of heterogeneous plastic flow at different structure-scale levels. We have investigated the stage of shear-band multiple development and have shown its important role in the deformation behavior of massive metallic glasses. We have also considered the effect of nanocrystals on the conditions of development and shear-band multiplication processes.

The unique combination of electromagnetic, corrosive, mechanical, and other specific properties of amorphous metallic alloys has led to their practical application in many branches of science and technology [1–4] and is responsible for the permanent attention given to these materials. Particular interest has been taken in bulk-amorphous alloys obtained as a result of the solidification of melts at low cooling rates (10^2–10^{-1} K s^{-1}) [2–4]. Nanocrystalline and amorphous-nanocrystalline materials obtained on the basis of massive amorphous metallic alloys have also garnered special attention [5]. These materials exhibit unique mechanical properties. Alloys that simply become amorphous and have nanocrystalline or quasi-nanocrystalline inclusions can possess both high strength and plasticity [6].

In order to discover the interconnection that exists between the structure and mechanical properties of bulk-amorphous metallic alloys, it is important to know the nature of their plastic strain. In this paper, we analyze the structural mechanisms of heterogeneous strain at different structure-scale levels, as well as the strain features of bulk-amorphous metallic alloys.

* *Baĭkov Institute of Metallurgy and Materials Science, Russian Academy of Sciences, Leninskiĭ pr. 49, Moscow, 112334 Russia*

** *Institute of Metal Physics and Functional Materials, Bardin Research Center TsNIIChermet, Vtoraya Baumanskaya ul. 9/23, Moscow, 107005 Russia*

e-mail: glezer@imph.msk.ru

STRUCTURAL-SCALE LEVELS FOR PLASTIC STRAIN OF AMORPHOUS ALLOYS

Under high stresses and at low temperatures ($T < 0.7T_g$, where T_g is the vitrification temperature), heterogeneous plastic flow is realized in amorphous metallic alloy whose strain is localized in thin shear bands [7, 8].

In [9], heterogeneous plastic flows of amorphous metallic alloys under high shear stresses were analyzed. The appearance of localized shears of small atomic groups referred to as shear transformations was considered to be the basic microstructural mechanism governing this phenomenon. These shears had the form of disk-shaped domains of a diameter $s = (4–6)a$, where a is the mean interatomic distance. In this case, the generation of a free volume occurs, which results in material softening and leads to the localization of material plastic flow in shear bands [9, 10]. Recent numerical studies [11] confirm the existence of this microscopic-level deformation mechanism.

The scale of the intermediate mesostructure-scale level of the heterogeneous plastic flow of amorphous metallic alloys is determined by the size of uncompleted shear bands (δ, 1) nucleating on stress concentrators, i.e., sample defects and alloy defects of average size h (Fig. 1a).

The conditions of shear-band development in amorphous metallic alloys were investigated in [10], in which a quantitative criterion for shear-band development was formulated. The condition for shear-band propagation can be written in terms of either the stress-intensity coefficient K_b ($K_b \geq K_{b1}^*$) for a band or the external stress τ. The criterion for the propagation of a band of length L can be written in the form

$$\tau_p - \tau_0 = \left[\frac{4\mu}{\pi(1-\nu)}\frac{(\tau_m[x_i]-\tau_0)u_e}{L}\right]^{1/2}. \qquad (1)$$

Here, u_e is the mean displacement at the end part of the band, τ_0 is the steady-state shear-resistance stress in the band, μ is the shear modulus, and ν is the Poisson's ratio. The stress τ_m depending on the degree of material

1028-3358/05/5008-0409$26.00

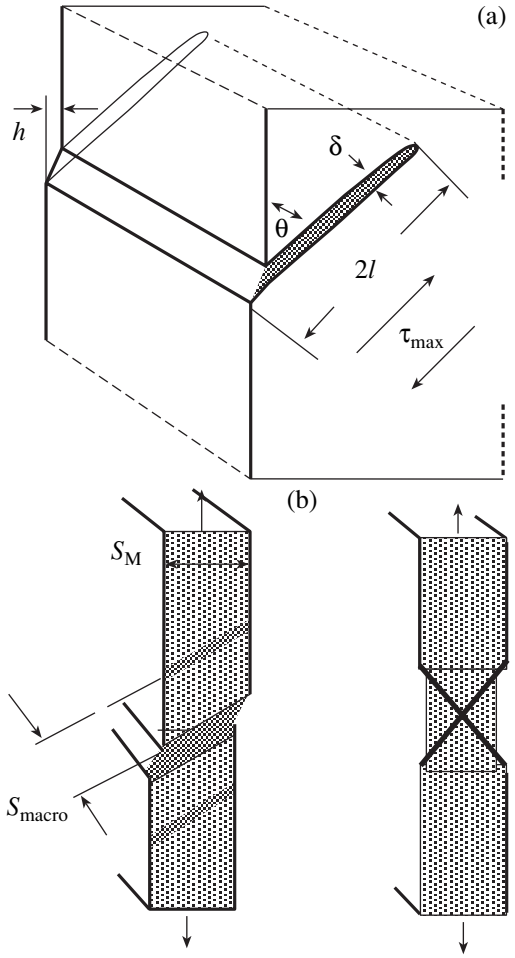

Fig. 1. Mechanisms of heterogeneous plastic strain of amorphous alloy: (a) the initial stage of the shear-band development and (b) completed shear bands.

homogeneity, and hence, on the spatial coordinates x_i is determined by the concentration levels $f_v(x_i)$ and $f_s(x_i)$ of the excess free volume and nanometer-size structural inhomogeneities, respectively. Relationship (1) determines the critical propagation stress for a band of the given size or the critical band size at a given external shear stress. Upon attaining a certain length, the shear bands formed are stopped due to their blocking on mesostructure inhomogeneities. The characteristic scale of structural processes is $S_m \sim 0.01$–1 μm.

The macroscopic condition for the development of a shear band in an amorphous metallic alloy, i.e., the condition of overcoming by a shear band obstacles caused by microstructure inhomogeneities can be represented by introducing the second critical value of the stress-intensity coefficient K^*_{b2} ($K^*_{b2} > K^*_{b1}$) for the bands:

$$K_b \geq K^*_{b2}. \quad (2)$$

The quantity K^*_{b2} is determined by the nature, size, and concentration of mesostructure inhomogeneities in amorphous metallic alloy.

In the case of strain of amorphous metallic alloys that are rendered amorphous with difficulty, only the initial stage in the development of uncompleted shear bands is realized when their interaction is insignificant (the exclusion is the strain under rolling a tape of amorphous metallic alloy). As a rule, shear bands are positioned at an angle of 45°–55° to the axis of uniaxial loading [7, 8]. The deformation process rapidly attains the third macroscopic level, whose scale is determined by the sample thickness. Under stretching tapes made of amorphous metallic alloy, the most intense of them occupy the entire sample, and intense plastic flow arises over several completed shear bands (Fig. 1b). This intermittent plastic flow is completed by opening cracks along the band [7, 8]. In this case, the characteristic scale of the macrostructure level is $S_M \sim 1$–40 μm.

MULTIPLE DEVELOPMENT OF SHEAR BANDS

We call shear bands formed at stress concentrators primary shear bands. The intrinsic feature of plastic strain for bulk amorphous metallic alloys that can easily be rendered amorphous is that of the formation of new secondary shear bands in the vertices of blocked primary ones. This results in the multiple development of shear bands (i.e., self-catalytic properties of the process manifest themselves) (see Fig. 2). We now analyze the kinetics of the process.

The volume fraction of primary shear bands formed at stress concentrators is f_b. An increase in the band volume fraction is proportional to the plastic strain ε_p. Under the assumption of a permanent generation rate of the shear bands and with allowance for the excess band volume, we may write the expression connecting the volume fraction of the bands with the plastic strain in the form

$$\frac{df_b}{(1-f_b)} = p_b d\varepsilon_p, \quad \tau \geq \tau^*. \quad (3)$$

Here, τ^* is the stress of the shear-band formation on a concentrator of maximum size for a given sample, and p_b is a parameter independent of ε_p and corresponding to the intensity of the primary-band formation at small ε_p. Hence, it follows that

$$f_b = 1 - \exp(-p_b\varepsilon_p), \quad \tau \geq \tau^*. \quad (4)$$

The number of primary shear bands per unit volume of amorphous metallic alloy is $N_b = \dfrac{f_b}{v_b}$, where v_b is the mean volume of a primary band.

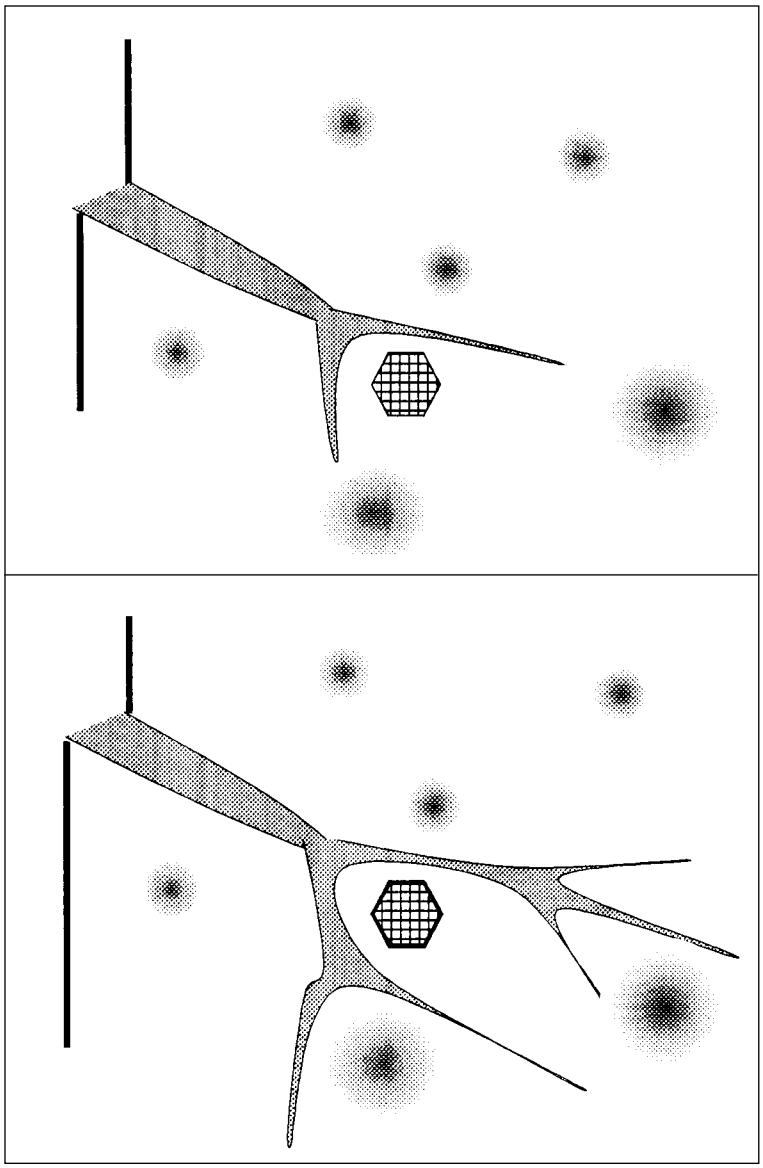

Fig. 2. Stage of the multiple development of shear bands in bulk-amorphous alloys.

The number N_s of secondary shear bands per unit volume is proportional to a certain power n of the primary-band number:

$$N_s = p_s(N_s)^n. \quad (5)$$

The parameters n and p_s are determined by the generation conditions for novel shear bands in the vertices of blocked ones. At the same time, the process of band multiplication leads to delocalization and, correspondingly, to hampering of the heterogeneous plastic flow:

$$df_s \sim (1 - \beta f_s)d\varepsilon_p, \quad (6)$$

where β is a certain numerical coefficient.

If the average volume of secondary shear bands is v_s, then the increase in the volume fraction f_s of the secondary shear bands is determined by the expression

$$f_s = \beta^{-1}[1 - \exp\{-\alpha[1 - \exp(-p_b\beta\varepsilon_p)]^n\}], \quad (7)$$

where $\alpha \equiv \dfrac{v_s p_p}{(v_b)^n}$. The dependence of the reduced volume fraction $f_s\beta$ of the bands on the plastic strain ε_p for $\alpha = 8$, $p_b\beta = 20$, and $n = 4$ is shown in Fig. 3.

The scale of the macrostructure level attains the sample thickness of the bulk-amorphous metallic alloy: $S_M \sim 10$ mm.

AN EFFECT OF NANOCRYSTALLINE INCLUSIONS ON THE DEVELOPMENT OF SHEAR BANDS

The effect of nanocrystals appearing in amorphous alloy upon the development of a heterogeneous flow of bulk-amorphous metallic alloys is twofold. On the one hand, they increase the resistance stress for the band development [12]. The critical stress for the shear-band development as a function of the volume fraction of disperse crystalline inclusions is of the form [12]

$$\tau_p \geq \left[\frac{4\mu(\tau_{m0} - \tau_0 + A\mu\varepsilon^* f)u_e}{\pi(1-\nu)L}\right]^{1/2}. \quad (8)$$

Here, f is the volume fraction of nanocrystals in amorphous metallic alloy, ε^* is the strain at the band front, which corresponds to the relative displacement u_e, and A is the numerical parameter on the order of unity.

When the size of crystalline particles is comparable with the shear-band thickness, the process of bending the band front between particles and changing the trajectory of its development is possible [12].

On the other hand, the probability of shear-band multiplication arises in amorphous metallic alloys containing nanocrystals. There are two structural mechanisms of the band development that are most probable, namely, the branching of bands blocked at nanometer-size inclusions and the nucleation of new bands in the vertices of blocked ones (Fig. 2). Hence, the presence of nanocrystals in an amorphous matrix results in the intensifying processes of band multiplication: $p_s = p_s(f)$.

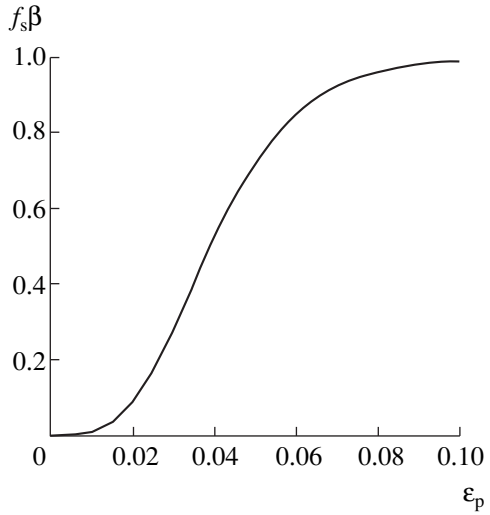

Fig. 3. Reduced volume fraction $f_s\beta$ of shear bands as a function of plastic strain ε_p.

STRAIN BEHAVIOR OF AMORPHOUS METALLIC ALLOYS

Different variants of the development of heterogeneous plastic flow and, correspondingly, different strain behaviors are possible. They depend on the structure state of the amorphous alloy, which is determined by the conditions of rendering the amorphous state, of the development of structural-relaxation processes, and of the sample loading.

The plastic strain ε_p is determined by the volume fraction of shear bands f_{sb} ($f_{sb} = f_b + f_s$) and by the average strain s in the bands:

$$d\varepsilon_p = f_{sb}ds + sdf_{sb}. \quad (9)$$

At the first stage of the heterogeneous-strain process, the formation and development of primary shear bands occurs, and the value of s depends on the acting stress, $s = s(\tau)$. The physical yield stress τ^* is determined by the distribution function $\Psi(\tau_3)$ for the stress τ_3 of the band formation.

The flow stress $\sigma(\varepsilon_p)$ of amorphous metallic alloy can be found as the mean value of the stress for the shear-band propagation in the given sample. If the distribution function for the shear-band propagation stress τ_p in amorphous metallic alloy is $\Phi(\tau_p)$, then the plastic-flow stress is

$$\sigma(\varepsilon_p) = m_p\int\Phi(\tau_p)d\tau_p + \sigma_i. \quad (10)$$

Here, m_p is the orientation factor, $\sigma_i(f_{sb}, f_s)$ is the internal stress stipulated by shear bands with volume fraction f_{sb} and by structure inhomogeneities with volume density f_s. At the second stage of the deformation process, the level of internal stresses depends, in the main, on the volume fraction of shear bands. At this stage, $s = \text{const}(\tau, \varepsilon_p)$, and the shape of the σ–ε curve is determined by the process of the shear-band multiple development.

Thus, in the present study, we have analyzed the mechanisms of heterogeneous plastic flow at different structure-scale levels for bulk metallic alloys that can be rendered amorphous. We have shown the crucial effect of the stage responsible for the multiple development of shear bands on the deformation behavior of massive metallic glasses. A model for the kinetics of shear-band multiplication has been proposed. The effect of nanocrystals in amorphous alloy on features of the development and multiplication of shear bands in massive amorphous alloys has also been considered.

REFERENCES

1. *Amorphous Metal Alloys*, Ed. by F. E. Lyuborskiĭ (Metallurgiya, Moscow, 1987) [in Russian].

2. V. V. Molokanov, E. B. Rubina, V. N. Chebotnikov, *et al.*, Fiz. Met. Metalloved. **68**, 964 (1989).
3. Yu. K. Kovneristyĭ, *Bulk-Amorphous Metal Alloys* (Nauka, Moscow, 1999) [in Russian].
4. S. Schneider, J. Phys.: Condens. Matter **13**, 7723 (2001).
5. Yu. K. Kovneristyĭ, Metally, No. 5, 19 (2001).
6. C. Fan, C. Li, and A. Inoue, Phys. Rev. B **61**, R3761 (2000).
7. A. M. Glezer and B. V. Molotilov, *Structure and Mechanical Properties of Amorphous Alloys* (Metallurgiya, Moscow, 1992) [in Russian].
8. V. P. Alekhin and V. A. Khonik, *Structure and Physical Mechanisms of Amorphous-Alloy Deformation* (Metallurgiya, Moscow, 1992) [in Russian].
9. A. S. Argon, Acta Metall. **27** (1), 47 (1979).
10. V. A. Pozdnyakov, Fiz. Met. Metalloved. **94** (5), 26 (2002) [Phys. Met. Metallogr. **94** (5), 443 (2002)].
11. M. L. Falk and J. S. Langer, Phys. Rev. E **57**, 7192 (1998).
12. V. A. Pozdnyakov, Fiz. Met. Metalloved. **97** (1), 9 (2004) [Phys. Met. Metallogr. **97** (1), 7 (2004)].

Translated by G. Merzon

Doklady Physics, Vol. 50, No. 8, 2005, pp. 414–418. Translated from Doklady Akademii Nauk, Vol. 403, No. 4, 2005, pp. 482–485.

MECHANICS

The Case of Complete Integrability in Three-Dimensional Dynamics of a Rigid Body Interacting with a Medium with the Inclusion of Rotary Derivatives of the Force Moment with Respect to the Angular Velocity

M. V. Shamolin

Presented by Academician V.V. Kozlov February 28, 2005

Received April 12, 2005

Due to its complexity, the problem of the motion of a rigid body in an unbounded medium requires the introduction of certain simplifying restrictions. The main aim in this connection is to introduce hypotheses that would make it possible to study the motion of the rigid body separately from the motion of the medium in which the body is embedded. On the one hand, a similar approach was realized in the classical Kirchhoff problem on the motion of a body in an unbounded ideal incompressible fluid that undergoes an irrotational motion and is at rest at infinity [1]. On the other hand, it is obvious that the above-mentioned Kirchhoff problem does not exhaust the possibilities of this kind of simulation.

In this paper, we consider the possibility of transferring the results of the dynamics of the plane-parallel motion of a homogeneous axisymmetric rigid body interacting with a uniform flow of a resisting medium through its forward circular face to the case of three-dimensional motion [2, 3]. In contrast to the preceding works (see also [4, 5]), the medium action on the rigid body is simulated with the inclusion of the effects of the so-called rotary derivatives of the moment of hydroaerodynamic forces with respect to the components of the angular velocity of the body itself [6, 7].

A DYNAMICALLY SYMMETRIC BODY UNDER THE ACTION OF THE NEWTONIAN DRAG AND A CONTROLLING FORCE

On the basis of certain hypotheses, the main one of which is the quasi-stationarity hypothesis, a three-dimensional dynamic model of the medium action on the body was developed. In this connection, the possibility arises to formalize the model assumptions and derive a complete system of equations.

As noted above, the medium–body interaction is concentrated on the body-surface part that has the shape of a plane circular disk. Under the assumption that the interaction obeys the jet flow laws [8, 9], the interaction force **S** is normal to the disk, while the application point N of the force **S** is determined by at least one parameter, namely, the angle of attack α between the velocity vector **v** of the center D of the disk and the outward normal at this point. Thus, we have $DN = R(\alpha, \ldots)$. We will take the magnitude of the Newtonian drag S in the form $S = s_1 v^2$, where the drag coefficient s_1 is a function of the angle of attack α only: $s_1 = s_1(\alpha)$.

At the same time, we will separate a class of problems related to the medium action on a body in which the controlling force acting along the geometrical symmetry axis ensures the realization of the classes of motions of interest under certain conditions [3, 10] (imposed constraints). Precisely the controlling force is a reaction of the constraints imposed. In the absence of a controlling force, the body undergoes three-dimensional free deceleration in a resisting medium (see also [11, 12]). In this study, the controlling force always ensures the fulfillment of the condition

$$|\mathbf{v}| = v = \text{const}. \tag{1}$$

In a body-fitted coordinate system, with one of the coordinate axes aligned with the axis of symmetry and two other axes lying in the plane of the disk, the tensor of inertia is diagonal: $\mathrm{diag}\{I_1, I_2, I_3\}$. Obviously, in this case we have

$$I_2 = I_3. \tag{2}$$

In order to describe the body position in the three-dimensional space, we will choose the cyclic Cartesian

Institute of Mechanics, Moscow State University, Michurinskiĭ pr. 1, Moscow, 119192 Russia
e-mail: shamolin@imec.msu.ru

1028-3358/05/5008-0414$26.00

coordinates of point D and three (also cyclic in our case) angles related, together with their velocities, by kinematic equations.

We will consider the spherical coordinates (v, α, β_1) of the end of the velocity vector $\mathbf{v}$ of the point D relative to the flow, where the angle β_1 is measured in the disk plane. Expressing the quantities (v, α, β_1) in terms of the cyclic kinematic variables and velocities via nonintegrable relations, we will consider them as quasivelocities supplementing them by the components $(\Omega_x, \Omega_y, \Omega_z)$ of the angular velocity in the body-fitted axes.

By virtue of Eq. (2) and the jet flow hypothesis, the following invariant relation, which is cyclic according to Routh, is always fulfilled:

$$\Omega_x = \Omega_{x_0} = \text{const}. \tag{3}$$

EQUATIONS OF MOTION IN THE CASE OF ZERO SPIN OF THE RIGID BODY ABOUT THE LONGITUDINAL AXIS

In what follows, we will investigate in more detail the case of zero spin of the rigid body about its longitudinal axis. In this case, the following condition is fulfilled:

$$\Omega_{x_0} = 0. \tag{4}$$

If $s(\alpha) = s_1(\alpha)\operatorname{sgn}\cos\alpha$, then the independent dynamic part of the equations of motion in the four-dimensional phase space has the form

$$\begin{aligned}&\dot{\alpha} v\cos\alpha\cos\beta_1 - \dot{\beta}_1 v\sin\alpha\sin\beta_1\\ &\quad + \Omega_z v\cos\alpha - \sigma\dot{\Omega}_z = 0,\end{aligned} \tag{5}$$

$$\begin{aligned}&\dot{\alpha} v\cos\alpha\sin\beta_1 + \dot{\beta}_1 v\sin\alpha\cos\beta_1\\ &\quad - \Omega_y v\cos\alpha + \sigma\dot{\Omega}_y = 0,\end{aligned} \tag{6}$$

$$I_2\dot{\Omega}_y = -z_N s(\alpha)v^2, \quad I_2\dot{\Omega}_z = y_N s(\alpha)v^2. \tag{7}$$

Here, σ is the distance from the center of mass to the plate and y_N and z_N are the Cartesian coordinates of the drag application point in the disk plane.

System (5)–(7) involves the medium action functions y_N, z_N, and s; for their qualitative determination, we will use the experimental information on the jet flow properties [4–9].

CHAPLYGIN FUNCTIONS OF MEDIUM ACTION

In what follows, we will address some typical "representatives" of the classes of the medium action functions under consideration, namely, the Chaplygin functions.

We will use Chaplygin's result as a reference point. Chaplygin calculated the medium action functions for an infinitely long plate in plane-parallel motion in the oncoming flow following the jet flow laws. In this case, the distance between the drag application point (center of pressure) and the plate center is proportional to the sine of the angle of attack, while the Newtonian drag coefficient multiplied by $\operatorname{sgn}\cos\alpha$ is proportional to its cosine [13].

Moreover, integrable cases in the dynamics of the three-dimensional motion of a rigid body were also found for other model problems in the early works of the present author [14]. For the Chaplygin medium action functions, the systems had a complete set of transcendental first integrals, which could be expressed in terms of a finite combination of elementary functions. In this case, transcendence is understood in the sense of the theory of functions of a complex variable (that is, their continuations to the complex plane have essentially singular points).

Thus, in what follows, we will restrict ourselves to the investigation of system (5)–(7) for the following medium action functions:

$$\begin{aligned}y_N &= A\sin\alpha\cos\beta_1 + h\frac{\Omega_z}{v},\\ z_N &= A\sin\alpha\sin\beta_1 - h\frac{\Omega_y}{v},\\ s(\alpha) &= B\cos\alpha, \quad A, B, h > 0,\end{aligned} \tag{8}$$

where the coefficient h occurs in terms that are proportional to the rotary derivatives of the moment of hydroaerodynamic forces with respect to the components of the angular velocity of the rigid body [6, 7].

A SYSTEM WITH VARIABLE DISSIPATION WITH ZERO MEAN VALUE AND AN ANALYTICAL RIGHT SIDE

System (5)–(7), including the case of Eq. (8), is a dynamic system with variable dissipation with zero mean value (over the angle of attack, in our case) [15]. This means that the integral over a period of the angle of attack from the divergence of its right-hand side is equal to zero [this integral is responsible for the phase volume variation (after the corresponding reduction of the system)]. In this sense, the system is "semiconservative."

Projecting then the angular velocities onto movable axes, which are unfitted to the body, so that

$$z_1 = \Omega_y \cos\beta_1 + \Omega_z \sin\beta_1, \quad z_2 = -\Omega_y \sin\beta_1 + \Omega_z \cos\beta_1, \tag{9}$$

and introducing dimensionless variables w_k, $k = 1, 2$, and parameters in accordance with the formulas $h_1 = hB$, $\frac{\sigma h_1}{I_2} = H_1$, $\beta = \sigma^2 \frac{AB}{I_2}$, and $\sigma z_k = \nu w_k$, where $\alpha' = \frac{\nu}{\sigma}\dot{\alpha}$, etc., we obtain the fourth-order dynamic system

$$\alpha' = -(1 + H_1)w_2 + \beta \sin\alpha, \tag{10}$$

$$w_2' = \beta \sin\alpha\cos\alpha - (1 + H_1)w_1^2 \frac{\cos\alpha}{\sin\alpha} - H_1 w_2 \cos\alpha, \tag{11}$$

$$w_1' = (1 + H_1)w_1 w_2 \frac{\cos\alpha}{\sin\alpha} - H_1 w_1 \cos\alpha, \tag{12}$$

$$\beta_1' = (1 + H_1)w_1 \frac{\cos\alpha}{\sin\alpha}, \tag{13}$$

which incorporates an independent third-order subsystem given by Eqs. (10)–(12).

For $\beta = H_1$, the divergence of the right-hand side of system (10)–(12), or (10)–(13), is identically zero after the change of variables $w_1^* = \ln|w_1|$; this property makes it possible to consider this system (these systems) as conservative.

Theorem 1. *System* (10)–(13) *possesses a complete set of first integrals being elementary transcendental functions of their phase variables. Two of them form a complete set of the first integrals of system* (10)–(13).

Indeed, we will associate system (10)–(13) with the second-order non-autonomous system

$$\frac{dw_2}{d\alpha} = \frac{\beta \sin\alpha\cos\alpha - (1 + H_1)w_1^2 \frac{\cos\alpha}{\sin\alpha} - H_1 w_2 \cos\alpha}{-(1 + H_1)w_2 + \beta \sin\alpha}, \tag{14}$$

$$\frac{dw_1}{d\alpha} = \frac{(1 + H_1)w_1 w_2 \frac{\cos\alpha}{\sin\alpha} - H_1 w_1 \cos\alpha}{-(1 + H_1)w_2 + \beta \sin\alpha}. \tag{15}$$

Applying the substitution $\tau = \sin\alpha$, we transform the system of Eqs. (14) and (15) to the form

$$\frac{dw_2}{d\tau} = \frac{\beta\tau - (1 + H_1)w_1^2 \frac{1}{\tau} - H_1 w_2}{-(1 + H_1)w_2 + \beta\tau}, \tag{16}$$

$$\frac{dw_1}{d\tau} = \frac{(1 + H_1)w_1 w_2 \frac{1}{\tau} - H_1 w_1}{-(1 + H_1)w_2 + \beta\tau}. \tag{17}$$

Making then the change $w_k = u_k\tau$, $k = 1, 2$, characteristic of homogeneous systems, we will associate the system specified by Eqs. (16) and (17) with the non-autonomous differential equation

$$\frac{du_2}{du_1} = \frac{\beta + (1 + H_1)(u_2^2 - u_1^2) - (H_1 + \beta)u_2}{2(1 + H_1)u_1 u_2 - (H_1 + \beta)u_1}, \tag{18}$$

which has a first integral of the form

$$\frac{(1 + H_1)u_2^2 - (H_1 + \beta)u_2 + (1 + H_1)u_1^2 + \beta}{u_1} = C_1. \tag{19}$$

In other words, system (10)–(12) has a first integral of the form

$$\frac{(1 + H_1)w_2^2 - (H_1 + \beta)w_2 \sin\alpha + (1 + H_1)w_1^2 + \beta \sin^2\alpha}{w_1 \sin\alpha} = C_1. \tag{20}$$

As noted above, at $\beta = H_1$ the dynamic system given by Eqs. (10)–(12), as well as system (10)–(13), is conservative. Indeed, Eq. (20) is transformed to the invariant relation

$$\frac{w_2^2 + (1 + \beta)w_1^2 + \beta[w_2 - \sin\alpha]^2}{w_1 \sin\alpha} = C_1. \tag{21}$$

Moreover, it is easy to verify that both the numerator and the denominator of Eq. (21) at $\beta = H_1$ are the first integrals of system (17)–(19):

$$w_2^2 + (1 + \beta)w_1^2 + \beta[w_2 - \sin\alpha]^2 = C_1^*, \quad w_1 \sin\alpha = C_2^*. \tag{22}$$

For $\beta \neq H_1$, system (10)–(12) is no longer conservative and neither the numerator nor the denominator of the invariant relation (20) is the first integral. This fact can not necessarily be verified analytically, because system (10)–(12) has attractive and repulsive limiting sets, which preclude the existence of the complete set of even continuous first integrals for the system under consideration.

The additional first integral for system (10)–(12) is obtained, by virtue of Eqs. (18) and (11), from the quadrature

$$\int \frac{d\tau}{\tau} = \int \frac{[\beta - (1 + H_1)u_2]du_2}{\beta - (H_1 + \beta)u_2 + (1 + H_1)[u_2^2 - U(u_1, C_1)]}, \quad (23)$$

where $U(u_1, C_1) = \frac{1}{2(1 + H_1)} \{C_1 \pm \sqrt{C_1^2 - 4D_1}\}$ on the level $C_1 > 4(1 + H_1)D_1$ of integral (21), where $D_1 = (1 + H_1)u_2^2 - (H_1 + \beta)u_2 + \beta$.

The general structural form of the additional first integral for system (10)–(12) is as follows:

$$\Phi_1(w_1, w_2, \sin\alpha) = C_2. \quad (24)$$

In view of Eqs. (13) and (17), the additional first integral for the fourth-order system given by Eqs. (10)–(13) is obtained from the solution of the equation

$$\frac{du_1}{d\beta_1} + \left[\frac{\beta - (1 + H_1)u_2}{1 + H_1}\right] = u_2 - \frac{H_1}{1 + H_1}, \quad (25)$$

which leads to the relation

$$\sin^2\{2(1 + H_1)^2(\beta_1 + C_3)\} = \frac{(2(1 + H_1)w_1 - 2C_1\sin\alpha)^2}{[(H_1 + \beta)^2 - 4\beta(1 + H_1) + C_1^2]\sin^2\alpha}. \quad (26)$$

THREE-DIMENSIONAL PENDULUM IN AN ONCOMING FLOW

By analogy with a free body, we will consider the problem of the motion of a three-dimensional pendulum in an oncoming uniform flow for the following case: the flow acts only on a circular disk fixed rigidly at its center, perpendicular to a sting that, in turn, is fixed by its other end on a spherical hinge. The model of the medium action on the disk is the same as above. The pendulum moves without its own spin. As before, the effects of the rotary derivatives of the moment of hydroaerodynamic forces with respect to the angular velocity of the rigid body are taken into account using the Chaplygin functions of the medium action.

If (ξ, η) are the angles determining the position of the three-dimensional pendulum on a sphere S^2, then the equations of motion of the system on the tangent bundle T_*S^2 of the two-dimensional sphere can be written in the form

$$\ddot{\xi} + (\beta - H_1)\dot{\xi}\cos\xi + \beta\sin\xi\cos\xi - \dot{\eta}^2\frac{\sin\xi}{\cos\xi} = 0, \quad (27)$$

$$\ddot{\eta} + (\beta - H_1)\dot{\eta}\cos\xi + \dot{\xi}\dot{\eta}\left[\frac{1 + \cos^2\xi}{\cos\xi\sin\xi}\right] = 0. \quad (28)$$

Here, β and H_1 are dimensionless physical constants and the coefficient H_1 is, as before, proportional to the rotary derivatives of the moment of hydroaerodynamic forces with respect to the components of the angular velocity of the three-dimensional pendulum. The sting length is equivalent to the distance σ and the constant velocity of the oncoming flow is equivalent to the constant parameter v. The angle of attack of the free body is equivalent to the angle ξ of the pendulum deviation from the flow velocity vector and the angle β_1 is equivalent to the cyclic variable (angle) η.

Theorem 2. *System* (10)–(12) *is topologically equivalent to the system given by Eqs.* (27) *and* (28).

We note that system (27), (28) for the case $\cos\xi = 0$ can be defined using continuity.

ACKNOWLEDGMENTS

This work was supported by the Russian Foundation of Basic Research, project no. 05-01-00401.

REFERENCES

1. H. Lamb, *Hydrodynamics*, 6th ed. (Cambridge University Press, Cambridge, 1932; Gostekhizdat, Moscow, 1947).
2. M. V. Shamolin, Dokl. Akad. Nauk **364** (5), 627 (1999) [Dokl. Phys. **44**, 110 (1999)].
3. M. V. Shamolin, Izv. Ross. Akad. Nauk, Mekh. Tverd. Tela, No. 2, 65 (1997).
4. B. Ya. Lokshin, V. A. Privalov, and V. A. Samsonov, *Introduction to the Problem of the Motion of a Body in a Resisting Medium* (Mosk. Gos. Univ., Moscow, 1986) [in Russian].

5. M. V. Shamolin, Vestn. Mosk. Univ., Ser. 1: Mat., Mekh., No. 5, 22 (2001).

6. G. S. Byushgens and R. V. Studnev, *Dynamics of Longitudinal and Lateral Motion* (Mashinostroenie, Moscow, 1969) [in Russian].

7. G. S. Byushgens and R. V. Studnev, *Aircraft Dynamics. Three-Dimensional Motion* (Mashinostroenie, Moscow, 1988) [in Russian].

8. S. A. Chaplygin, *Selected Papers* (Nauka, Moscow, 1976) [in Russian].

9. M. I. Gurevich, *Theory of Ideal Fluid Flows* (Nauka, Moscow, 1979) [in Russian].

10. V. A. Samsonov and M. V. Shamolin, Vestn. Mosk. Univ., Ser. 1: Mat., Mekh., No. 3, 51 (1989).

11. M. V. Shamolin, Dokl. Akad. Nauk **371** (4), 480 (2000) [Dokl. Phys. **45**, 171 (2000)].

12. M. V. Shamolin, Vestn. Mosk. Univ., Ser. 1: Mat., Mekh., No. 4, 57 (1996).

13. S. A. Chaplygin, in *Complete Works* (Akad. Nauk SSSR, Leningrad, 1933), Vol. 1, pp. 133–135 [in Russian].

14. M. V. Shamolin, Vestn. Mosk. Univ., Ser. 1: Mat., Mekh., No. 1, 52 (1992); No. 1, 112 (1992).

15. M. V. Shamolin, Usp. Mat. Nauk **54** (5), 181 (1999).

Translated by M. Lebedev

Doklady Physics, Vol. 50, No. 8, 2005, pp. 419–422. Translated from Doklady Akademii Nauk, Vol. 403, No. 5, 2005, pp. 627–630.

MECHANICS

Experimental Studies of Turbulent Helicity and Its Spectrum in the Atmospheric Boundary Layer

B. M. Koprov*, V. M. Koprov*, V. M. Ponomarev*, and O. G. Chkhetiani**

Presented by Academician G.S. Golitsyn April 18, 2005

Received April 20, 2005

1. In this paper, we present results of the first measurements of turbulent helicity in the atmospheric boundary layer. The spectra obtained are analyzed within the framework of the problem of helicity turbulent cascades towards small scales. For the scales being considered in this study, the helicity spectrum turns out to be similar to the passive-admixture spectrum.

Helicity is defined as a scalar product of the velocity $\mathbf{v}$ and the vorticity: $\boldsymbol{\omega} = \nabla \times \mathbf{v}$. A difference of helicity from zero implies the violation of the flow mirror symmetry that exists, e.g., in the Ekman's atmospheric boundary layer. Helicity plays a significant role in processes of magnetic-fields generation in a conducting liquid, and it is one of the important characteristics of large-scale atmospheric motions [1–5]. At the same time, the role of helicity in hydrodynamic turbulence has not yet been entirely revealed, although we may assume that the turbulization of spiral flows results in the helicity of turbulent velocity pulsations. Within the inviscid limit, the Navier–Stokes equations conserve kinetic energy and helicity. For turbulent flows, the presence of two quadratic invariants indicates the possible existence of both double cascades (when cascades of the energy and helicity are realized in different segments of wave numbers by analogy with the two-dimensional turbulence) and the helicity cascade in parallel with the energy cascade towards small scales [6]. In particular, the existence of the exact relation connecting double and triple velocity correlations, which was later referred to as the 2/15 law (by analogy with Kolmogorov's 4/5 law) [7], is associated with the helicity cascade.

In accordance with [6], the above-indicated scenarios of turbulent cascades exhibit different spectral scalings. In the case of isotropic turbulence, parallel cascades of the energy $E = \frac{1}{2}\langle \mathbf{v}^2 \rangle$ and helicity $H = \langle \mathbf{v}\boldsymbol{\omega} \rangle$ towards small scales correspond to the spectra

$$E(k) = \frac{1}{2}\langle \mathbf{v}(k)\mathbf{v}^*(k) \rangle = C_e \varepsilon^{2/3} k^{-5/3},$$

$$H(k) = \langle \mathbf{v}(k)\boldsymbol{\omega}^*(k) \rangle = C_h \eta \varepsilon^{-1/3} k^{-5/3}.$$

In the case of double cascades, they correspond to the spectra

$$E(k) = c_e \eta^{2/3} k^{-7/3}, \quad H(k) = c_h \eta^{2/3} k^{-4/3}.$$

Here, $\mathbf{v}(k) = \sum_{|\mathbf{k}| = k} \mathbf{v}(\mathbf{k})$, $\boldsymbol{\omega}(k) = \sum_{|\mathbf{k}| = k} \boldsymbol{\omega}(\mathbf{k})$ are, respectively, the Fourier components of the velocity and vorticity; $\varepsilon = \nu \left\langle \frac{\partial \omega_i}{\partial x_k} \frac{\partial \omega_i}{\partial x_k} \right\rangle$ and $\eta = 2\nu \left\langle \frac{\partial v_i}{\partial x_k} \frac{\partial \omega_i}{\partial x_k} \right\rangle$ are the dissipation rates for the turbulent energy and helicity, respectively; ν is the kinematic viscosity; and $\mathbf{k}$ is the wave number.

The theoretical arguments of Kraichnan [8] and the results of numerical simulations [9–11] of Navier–Stokes equations uphold the realization of the parallel-cascade scenario. In the present study, we carry out measurements of the velocity and vorticity, which allow us to experimentally estimate the spectrum of the turbulent helicity in the atmospheric boundary layer. The results obtained show that the spectrum has a slope of close to –5/3, which corresponds to the helicity transfer over the spectrum towards small scales analogously to a passive scalar. This implies that the helicity slightly affects small-scale motions. At the same time, the existence of the helicity flux of only one sign weakens the energy cascade associated with modes of the other sign [11].

* *Obukhov Institute of Atmospheric Physics, Russian Academy of Sciences, Pyzhevskiĭ per. 3, Moscow, 119017 Russia*

** *Space Research Institute, Russian Academy of Sciences, Profsoyuznaya ul. 84/32, Moscow, Russia*

1028-3358/05/5008-0419$26.00

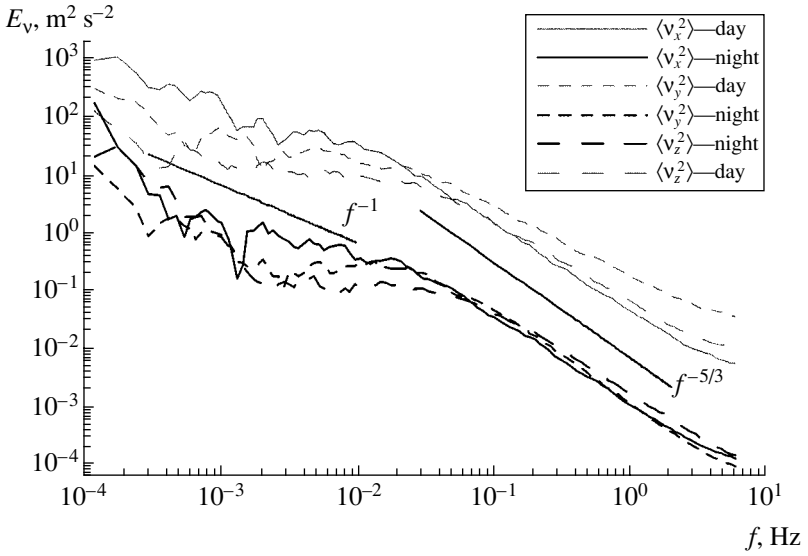

Fig. 1. Frequency spectra for velocity components.

The balance of turbulent helicity H in the atmospheric boundary layer can be described by the equation

$$\frac{dH}{dt} = \frac{\partial\langle v_i v_k\rangle}{\partial x_k}\Omega_i - \langle v_i v_k\rangle\frac{\partial\Omega_i}{\partial x_k} + 2\Omega_{0i}\frac{\partial E}{\partial x_i} + 2\beta\langle\theta\omega_z\rangle,$$

$$-\frac{\partial}{\partial x_k}\left\langle\frac{p}{\rho}\omega_k + v_i v_k\omega_i - \frac{1}{2}\omega_k v_i v_i\right\rangle + \nu\Delta H - \eta,$$

whence it follows the estimate [5]

$$H = 2K\tau\,\boldsymbol{\Omega}\cdot(\nabla\times\boldsymbol{\Omega}) - \Omega_0\tau\frac{dE}{dz}F(\mathrm{Ri}).$$

Here, K is the turbulent viscosity, $\boldsymbol{\Omega} = \nabla\times\mathbf{V}$ is the large-scale vortex, Ω_0 is the angular velocity of the Earth's rotation, β is the buoyancy parameter, θ is the temperature pulsation, $F(\mathrm{Ri})$ is the function of the Richardson number, $\tau = \dfrac{l}{E^{1/2}}$, and l is the turbulence characteristic scale.

Thus, the turbulent-helicity density in the boundary layer close to the neutral one is estimated as $H \approx 3\times 10^{-3}$–$2\times 10^{-2}$ m s^{-2}.

2. Experiments aimed at the measurement of helicity spectral characteristics are extremely rare. They have been carried out under laboratory conditions only (the experiments were performed in solutions of weak electrolytes, which was stipulated by the measurement methods used) in turbulence beyond a grid [12], where nonzero averaged-helicity values were observed.

For experimental helicity estimates, it is necessary to measure all three components of the velocity and of the vortex. The direct estimation of the vortex according to the velocity fields is at present a rather complicated task. At the same time, while measuring the circulation along the given contour, namely,

$$Z = \oint\mathbf{v}d\mathbf{l} = \int\omega_n ds,$$

we can obtain a quite acceptable accuracy for the area-averaged vorticity. The concept of the acoustical method of vorticity measurements and the first results of its realization are described in [13]. This method consists in measuring the time that is required for a sound signal to pass along a closed contour. In addition to the wind-velocity circulation, this time also depends on the temperature inhomogeneity along the contour, whose effect can be estimated by comparing the results obtained for two opposite path tracings. In these spectral measurements, the other sources of systematic error are the vorticity averaging over the contour area and the spatial displacement of the points for measuring the velocity and the vortex.

In [14, 15], estimates of the effects indicated and measured results are given for the circulation spectra and co-spectra of certain components of the vortex-flux tensor in the atmospheric surface layer. In the same papers, the latter are compared with theoretical predictions that are based on the assumption of the mirror symmetry of flow characteristics with respect to reflections in the vertical plane parallel to the direction of the average velocity. The deviation from zero of covariances $\langle v_3 Z_2\rangle$ and $\langle v_1 Z_2\rangle$, which are associated with the circulation in the vertical plane parallel to the average flow, is explicitly consistent with this theory. In addi-

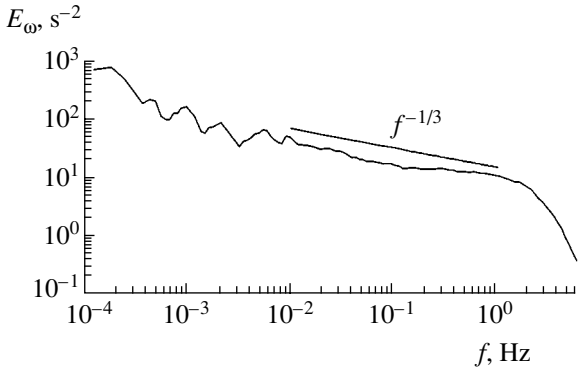

Fig. 2. Frequency spectra for the enstrophy.

tion, a strong correlation of the circulation field with the temperature field was found.

In the present study, based on a novel version of the three-component circulation meter, we have performed combined measurements of the circulation components, velocity, and temperature in the atmospheric boundary layer at an altitude of 46 m. At this altitude, it is expected that the effect of the local inhomogeneities of the underlying surface will be weakened. On the other hand, the wind turn stipulated by the Earth's rotation must manifest itself more noticeably with increasing altitude.

The measurements were carried out at the Zvenigorod scientific station of the Institute of Atmospheric Physics in September 2004. Circulation was measured using a quadratic contour with side lengths of 0.5 m. The distance between a velocity-measurement point and the contour center was about 1 m. The experimental data were registered by a 14-digital transformer with a sampling frequency of up to hundreds of Hertz. The total time duration for the measurements attained more than 70 h.

3. In conclusion, we present the results of the analysis of the experimental data for two two-hour realizations. The first of these relates to daily measurements in a weakly convective boundary layer, whereas the second one corresponds to nightly measurements when the boundary layer passed toward the stable state. Figures 1 and 2 exhibit the autospectra for temporal variations of the velocity components and of the enstrophy (vorticity squared) in the case of a weakly convective boundary layer. The features of the velocity spectra obtained are typical of the atmosphere boundary layer at such altitudes. We note a steepening in the enstrophy spectrum near the frequency $f \approx 1$ Hz. This frequency approximately corresponds to the wave numbers for which pulsations begin to be averaged by the contours.

The power spectrum of helicity fluctuations in a daily boundary layer is shown in Fig. 3. It is worth noting that this spectrum is highly consistent with the scaling $E_H(f) \sim f^{-1/3}$, which corresponds to the Kolmogorov theory and is based on the assumption that the spectrum is determined solely by the energy-dissipation rate ε.

The spectra of vertical and horizontal helicity components for the daily and nightly boundary layers are given in Fig. 4. For comparison, the slope of –5/3 is shown in the figure. As is seen, the slopes of the helicity spectrum components are close to this value. The integral estimate of the helicity according to its spectrum yields a value of 0.02–0.03 m s^{-2}, which coincides in terms of the order of magnitude with above-mentioned theoretical estimates. It is of interest to note that these values of helicity are close to those for characteristic secondary structures of the atmospheric boundary layer, the so-called rolls [1].

The data obtained for both the values of turbulent helicity in the atmospheric boundary layer and helicity spectra indicate the existence, at least in the region of the scales that have been considered, of parallel cascades of the energy and helicity. This also implies the possibility of the realization of certain effects following from the models of turbulent flows and taking into account turbulent helicity [4, 5]. The importance of the determination of actual helicity cascades in natural sys-

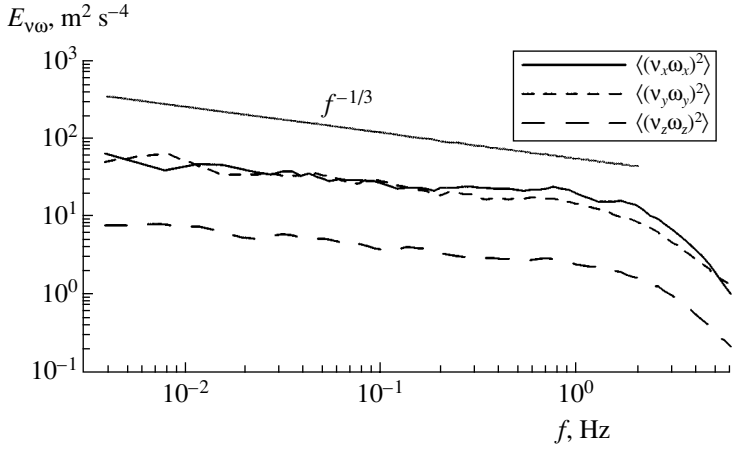

Fig. 3. Frequency spectra of helicity fluctuations.

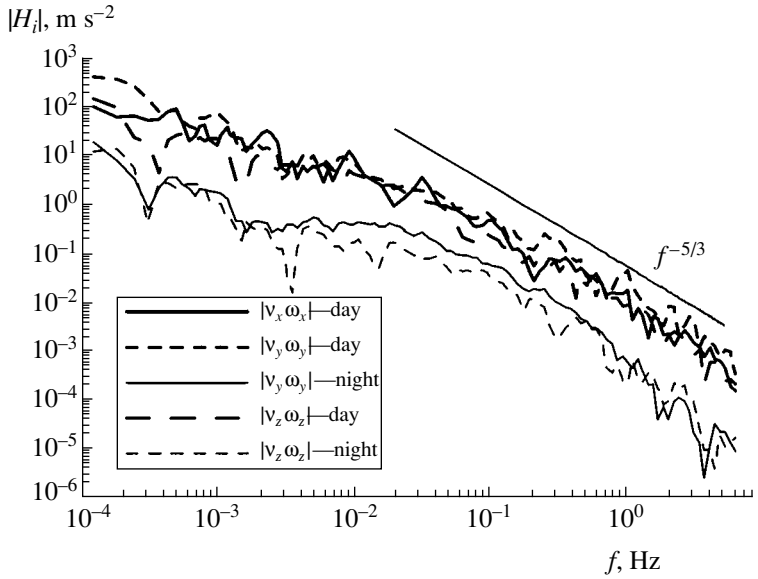

Fig. 4. Spectra of helicity components.

tems is also stipulated by the fact that some numerical calculations of the Navier–Stokes equations manifest certain effects of nonzero helicity on the energy transfer over the spectrum. This emphasizes the role of helicity in the formation of large-scale structures.

ACKNOWLEDGMENTS

The authors would like to thank G.V. Azizyan for the development of the scheme for velocity-circulation measurements, as well as V.A. Bezverkhniĭ for his help in the data treatment. The authors also are grateful to G.S. Golitsyn for fruitful discussions.

This study was supported by the Russian Foundation for Basic Research, project nos. 03-05-64593, 04-05-79160, and 05-05-64735.

REFERENCES

1. D. Etling, Beitr. Phys. Atmosph. **58**, 88 (1985).
2. H. K. Moffat and A. Tsinober, Annu. Rev. Fluid Mech. **24**, 281 (1992).
3. M. V. Kurganskiĭ, *Introduction to Large-Scale Dynamics of Atmosphere. Adiabatic Invariants and Their Application* (Gidrometeoizdat, St. Petersburg, 1993) [in Russian].
4. V. M. Ponomarev, A. A. Khapaev, and O. G. Chkhetiani, Izv. Ross. Akad. Nauk, Fiz. Atmos. Okeana **39** (4), 435 (2003) [Izv., Atmos. Ocean. Phys. **39** (4), 391 (2003)].
5. V. M. Ponomarev and O. G. Chkhetiani, Izv. Ross. Akad. Nauk, Fiz. Atmos. Okeana **41** (4) (2005) (in press).
6. A. Brissaud, U. Frisch, J. Leorat, *et al.*, Phys. Fluids **16**, 1363 (1973).
7. O. G. Chkhetiani, Pis'ma Zh. Éksp. Teor. Fiz. **63**, 768 (1996) [JETP Lett. **63**, 808 (1996)].
8. R. H. Kraichnan, J. Fluid Mech. **59**, 745 (1973).
9. J. C. Andre and M. Lesieur, J. Fluid Mech. **81**, 187 (1977).
10. V. Borue and S. A. Orszag, Phys. Rev. E **55**, 7005 (1997).
11. Q. Chen, S. Chen, and G. L. Eyink, Phys. Fluids **15**, 361 (2003).
12. M. Kholmyansky, M. Shapiro-Orot, and A. Tsinober, Proc. R. Soc. London, Ser. A **457**, 2699 (2001).
13. V. M. Bovsheverov, A. S. Gurvich, A. N. Kochetkov, *et al.*, Izv. Akad. Nauk SSSR, Fiz. Atmos. Okeana **7** (4), 371 (1971).
14. B. M. Koprov, G. V. Azizyan, and V. V. Kalugin, Izv. Akad. Nauk SSSR, Fiz. Atmos. Okeana **23**, 1151 (1987).
15. B. M. Koprov, V. V. Kalugin, and N. S. Time, Izv. Ross. Akad. Nauk, Fiz. Atmos. Okeana **30**, 13 (1994).

Translated by G. Merzon

Doklady Physics, Vol. 50, No. 8, 2005, pp. 423–425. Translated from Doklady Akademii Nauk, Vol. 403, No. 6, 2005, pp. 761–763.

MECHANICS

Model of a Multicomponent Medium

V. F. Kuropatenko

Presented by Academician B.V. Litvinov June 25, 2004

Received September 9, 2004

The available models of multicomponent media (MCM) were described in the most general form in [1, 2]. The following statements made in those works had a large effect on the development of MCM models: first, balance conservation equations in their general form are of little interest for the mechanics of mixtures, and, second, the main problem in the mathematical simulation of multiphase mixtures is to derive a closed system of equations both for given physical and chemical properties of each individual phase and for a given structure for the mixture as a whole. In the 20–25 years that have elapsed since the appearance of the aforementioned publications, many works have been devoted to the development of particular models based on certain specifications. So far, the problem of deriving the conservation laws for a mixture from those for individual components, as well as the problem of the closure of the system of equations for the *i*th component, remains unsolved in the general case.

CONSTRAINTS

Each component i of a mixture of N components conserves the chemical attributes of the substance irrespective of its mass and is characterized by the following physical parameters: the pressure P_i, the density ρ_i, the specific internal energy E_i, the velocity $\mathbf{U}_i$, the temperature T_i, etc. The thermodynamic parameters obey the equation of state for the ith component. After the physical parameters have been changed to the partial quantities $\alpha_i P_i$, $\alpha_i\rho_i$, $\alpha_i\rho_i\mathbf{U}_i$, $\alpha_i\rho_i E_i$, etc., which are continuous in the (t, x_k) space ($k = 1, 2, 3$), each component turns out to be a continuous medium in the entire space occupied by the mixture, so that mass, momentum, and energy conservation laws can be written for it in the form of differential equations. Thus, all components of the mixture are simultaneously present at each point of the (t, x_k) space.

To clarify the essence of the MCM model proposed, we consider ideal compressible media that are free of heat conduction, chemical reactions, and field effects and have zero deviator of the stress tensor. This consideration does not lead to any loss of generality of the model, because all the above physical processes can be incorporated into the conservation laws for the components if necessary.

INTERACTION OF COMPONENTS

Type 1. Pairwise interaction. Let the ith and jth components interact with each other independently of other components. Then the momentum (R_{ij}) and energy (Φ_{ij}) flux densities satisfy the equation

$$\mathbf{R}_{ij} = -\mathbf{R}_{ji}, \quad \Phi_{ij} = -\Phi_{ji}. \tag{1}$$

The order of the subscripts indicates the interaction direction. We will multiply Eq. (1) by α_j and sum over j under the condition that $\mathbf{R}_{ii} = 0$ and $\Phi_{ii} = 0$. The result is marked by the subscript 0:

$$\sum_{j=1}^{N} \alpha_j \mathbf{R}_{ij} = \mathbf{R}_{i0} = -\mathbf{R}_{0i}, \quad \sum_{j=1}^{N} \alpha_j \Phi_{ij} = \Phi_{i0} = -\Phi_{0i}. \tag{2}$$

Multiplying Eq. (2) by α_i, summing over i, and taking Eq. (1) into account, we obtain

$$\begin{aligned} \sum_{i=1}^{N} \alpha_i \mathbf{R}_{i0} &= \sum_{i=1}^{N}\sum_{j=1}^{N} \alpha_i\alpha_j \mathbf{R}_{ij} = 0, \\ \sum_{i=1}^{N} \alpha_i \Phi_{i0} &= \sum_{i=1}^{N}\sum_{j=1}^{N} \alpha_i\alpha_j \Phi_{ij} = 0. \end{aligned} \tag{3}$$

The quantities $\mathbf{R}_{i0}$ and Φ_{i0} are the sums of the independent intensities of the momentum and energy fluxes from the ith component to all N components. The pairwise interaction is taken into account in the conservation laws for the ith component in almost all MCM models (see, e.g., [1–4]).

Type 2. Cluster interaction. In terms of the partial parameters $\alpha_i P_i$, $\alpha_i\rho_i$, $\alpha_i\rho_i\mathbf{U}_i$, $\alpha_i\rho_i E_i$, etc., a virtual con-

Russian Federal Nuclear Center VNIITF, Snezhinsk, Chelyabinskaya oblast, 454070 Russia
e-mail: V.F.Kuropatenko@vniitf.ru, domkur@snz.ru

1028-3358/05/5008-0423$26.00

tinuum (VC) can be introduced with the parameters

$$P = \sum_{i=1}^{N} \alpha_i P_i, \quad \rho = \sum_{i=1}^{N} \alpha_i \rho_i, \quad \rho \mathbf{U} = \sum_{i=1}^{N} \alpha_i \rho_i \mathbf{U}_i, \quad \rho E = \sum_{i=1}^{N} \alpha_i \rho_i E_i, \tag{4}$$

which are continuous in the space occupied by the mixture. The forces and fluxes associated with the VC will be marked by the subscript *s*. The mixture and VC are nonequilibrium if one of the following conditions is not fulfilled:

$$P_i = P_p, \quad \mathbf{U}_i = \mathbf{U}_p, \quad T_i = T_p, \quad P = P_p, \quad T = T_p,$$

where P_p, $\mathbf{U}_p$, and T_p are the equilibrium state parameters. In the process of relaxation, the parameters of the components and VC change, because $\mathbf{U}$, P, ρ, and E are determined by Eq. (4). The interaction between the *i*th component and the VC will be called the cluster interaction. By analogy with Eq. (2), the forces and energy fluxes associated with the cluster interaction are related by the equations

$$\mathbf{F}_{ksi} = -\mathbf{F}_{kis}, \quad \mathbf{Q}_{si} = -\mathbf{Q}_{is}, \quad \mathbf{F}_{k0s} = \sum_{i=1}^{N} \alpha_i \mathbf{F}_{kis}, \quad \mathbf{Q}_{0s} = \sum_{i=1}^{N} \alpha_i \mathbf{Q}_{is}. \tag{5}$$

CONSERVATION LAWS

We write the conservation laws for the *i*th component:

$$\frac{\partial}{\partial t}(\alpha_i \rho_i) + \nabla(\alpha_i \rho_i \mathbf{U}_i) = 0, \tag{6}$$

$$\frac{\partial}{\partial t}(\alpha_i \rho_i \mathbf{U}_i) + \frac{\partial}{\partial x_k}(\alpha_i \rho_i U_{ki} \mathbf{U}_i) + \nabla \alpha_i P_i + \frac{\partial}{\partial x_k}(\alpha_i \mathbf{F}_{ksi}) - \alpha_i \mathbf{R}_{0i} = 0, \tag{7}$$

$$\frac{\partial}{\partial t}(\alpha_i \rho_i \varepsilon_i) + \nabla(\alpha_i \mathbf{U}_i (P_i + \rho_i \varepsilon_i)) + \frac{\partial}{\partial x_k}(\alpha_i \mathbf{F}_{ksi} \mathbf{U}_i) + \nabla \alpha_i \mathbf{Q}_{si} - \alpha_i \Phi_{0i} = 0. \tag{8}$$

In view of Eqs. (2), (3), and (5), the conservation laws for the VC are written in the form

$$\frac{\partial \rho}{\partial t} + \nabla \rho \mathbf{U} = 0, \tag{9}$$

$$\frac{\partial}{\partial t}(\rho \mathbf{U}) + \frac{\partial}{\partial x_k}(\rho U_k \mathbf{U}) + \nabla P + \frac{\partial}{\partial x_k}(\mathbf{F}_{k0s}) = 0, \tag{10}$$

$$\frac{\partial}{\partial t}(\rho \varepsilon) + \nabla(\mathbf{U}(P + \rho \varepsilon)) + \frac{\partial}{\partial x_k}(\mathbf{U} \mathbf{F}_{k0s}) + \nabla Q_{0s} = 0. \tag{11}$$

FORCE

We consider the following equation obtained by substituting Eq. (4) into Eq. (9):

$$\sum_{i=1}^{N} \left(\frac{\partial}{\partial t}(\alpha_i \rho_i) + \nabla(\alpha_i \rho_i \mathbf{U}_i) \right) = 0.$$

Each term in this sum is equal to zero, because it coincides with the left-hand side of Eq. (6). Thus, the summation of Eq. (6) yields Eq. (9).

Substituting Eqs. (2)–(5) into Eq. (10), we obtain

$$\sum_{i=1}^{N} \left(\frac{\partial}{\partial t}(\alpha_i \rho_i \mathbf{U}_i) + \frac{\partial}{\partial x_k}(\alpha_i \rho_i U_{ki} \mathbf{U}_i) + \nabla \alpha_i P_i + \frac{\partial}{\partial x_k}(\alpha_i \mathbf{F}_{kis}) - \alpha_i \mathbf{R}_{0i} \right) = 0. \tag{12}$$

We choose $\mathbf{F}_{ksi}$ so that each term in Eq. (12) coincides with Eq. (7). After simple transformations, we obtain the following expression for the force $\mathbf{F}_{ksi}$:

$$\mathbf{F}_{ksi} = 0.5 \rho_i (U_{ki} - U_k)(\mathbf{U} - \mathbf{U}_i). \tag{13}$$

NONEQUILIBRIUM KINETIC ENERGY

We consider the specific total energies of the VC and the *i*th component:

$$\varepsilon = E + 0.5 \mathbf{U}\mathbf{U} + H, \quad \varepsilon_i = E_i + 0.5 \mathbf{U}_i \mathbf{U}_i. \tag{14}$$

Expressing E and E_i from Eq. (14) and substituting the result into the fourth of Eqs. (4), we obtain

$$\rho H = \sum_{i=1}^{N} \alpha_i \rho_i H_i, \tag{15}$$

where H_i is determined by the equation

$$H_i = 0.5(\mathbf{U} - \mathbf{U}_i)^2. \tag{16}$$

We will call this quantity the nonequilibrium kinetic energy of the *i*th component.

ENERGY FLUX

The substitution of Eqs. (2)–(5), (13), and (15) into Eq. (11) yields

$$\sum_{i=1}^{N}\left(\frac{\partial}{\partial t}(\alpha_i\rho_i\varepsilon_i) + \nabla(\alpha_i(\mathbf{U}(P_i + \rho_i\varepsilon_i) - \mathbf{Q}_{si})) - \frac{\partial}{\partial x_k}(\alpha_i\mathbf{F}_{ksi}\mathbf{U}) - \alpha_i\Phi_{0i}\right) = 0. \quad (17)$$

The condition that the ith term in Eq. (17) coincides with Eq. (8) is as follows:

$$\mathbf{Q}_{si} = 0.5(P_i + \rho_i H_i)(\mathbf{U} - \mathbf{U}_i). \quad (18)$$

Requiring that the increment of the entropy of the mixture is equal to the sum of the increments of the entropies of the components, we arrive at the equation for volume concentration:

$$P_i\frac{d_i\ln\alpha_i}{dt} + \alpha_i\Phi_{si} - (\mathbf{U} - \mathbf{U}_i)\rho_i E_i\nabla\alpha_i - \alpha_i\left(E_i + \frac{P_i}{\rho_i}\right)\nabla\rho_i(\mathbf{U} - \mathbf{U}_i) = 0. \quad (19)$$

Equation (19) closes the system of equations for the ith component.

New forces $\mathbf{F}_{ksi}$ (13) and energy fluxes $\mathbf{Q}_{si}$ (18) include the parameters of the structural MCM level (mesolevel) with the subscript i and the barycentric velocity $\mathbf{U}$, which is a macrolevel parameter. This structure is typical of mesomechanical equations. These forces and fluxes vanish at velocity equilibrium.

The technique for obtaining $\mathbf{F}_{ksi}$ and $\mathbf{Q}_{si}$ is such that the conservation laws for the VC are derived by summing the conservation laws for the components.

COMPLETE EQUATIONS OF THE MODEL

The system of equations governing the behavior of the ith component includes the conservation laws given by Eqs. (6)–(8); the second of Eqs. (14); Eq. (19) for the function α_i given by Eq. (19); the equations of state $P_i = P_i(\rho_i, E_i)$ and $T_i = T_i(\rho_i, E_i)$; Eqs. (13) and (18) for the force $\mathbf{F}_{ksi}$ and energy flux $\mathbf{Q}_{si}$, respectively; the expression for the intensities of the exchange by the momentum $\mathbf{R}_{0i}$ and the energy Φ_{0i}; and Eqs. (4) for P, ρ, and $\mathbf{U}$. Thus, the complete system of equations for the mixture contains the same number of equations and functions and is closed without any additional hypotheses specifying the mixture.

ACKNOWLEDGMENTS

This work was supported by the International Science and Technology Center, grant no. 1181, and the Russian Foundation for Basic Research, project no. 04-01-00050.

REFERENCES

1. A. N. Kraĭko, R. I. Nigmatulin, V. K. Starkov, and L. B. Sternin, Itogi Nauki Tekh., Ser.: Gidromekh. **6**, 93 (1973).
2. R. I. Nigmatulin, *Fundamentals of Mechanics of Heterogeneous Media* (Nauka, Moscow, 1978) [in Russian].
3. N. N. Yanenko, R. I. Soloukhin, A. N. Papyrin, and V. M. Fomin, *Supersonic Two-Phase Flows Under the Conditions of Velocity Nonequilibrium of Particles* (Nauka, Novosibirsk, 1980) [in Russian].
4. V. F. Kuropatenko, Mat. Model. **1** (2), 118 (1989).

Translated by M. Lebedev

Doklady Physics, Vol. 50, No. 8, 2005, pp. 426–429. Translated from Doklady Akademii Nauk, Vol. 403, No. 6, 2005, pp. 764–767.

MECHANICS

Gravity–Capillary Waves on the Surface of a Liquid Dielectric

V. G. Meledin, V. A. Pavlov, O. Yu. Tsvelodub, and N. I. Yavorskiĭ*

Presented by Academician A.K. Rebrov January 31, 2005

Received February 21, 2005

Waves on the surface of a liquid dielectric layer in an alternating electric field are studied both experimentally and theoretically. The experiments reveal the characteristic patterns of standing waves forming rectangular and hexagonal cells—quasicrystalline wave structures. The shapes and sizes of these cells are studied as functions of the intensity and frequency of the electric field. The theoretical analysis is performed in the linear approximation. Equations are derived that describe the dynamics of standing waves in arbitrarily thick layers of both ideal and viscous fluids. Theory is in good quantitative and qualitative agreement with experiments.

The problem concerning the excitation of waves on the surface of a liquid-dielectric layer was first studied long ago [1, 2]. However, a complete linear theory of wave formation on the viscous-fluid surface has not yet been developed for any thicknesses of the dielectric layer or any wavenumbers. Experimental studies of such phenomena have been constrained by the absence of appropriate measuring instruments for the mathematical processing of measured wave structures.

In this work, we consider a linear problem of the generation of waves on the surface of an infinite horizontal dielectric layer situated inside a plane capacitor. The dielectric is placed in the parallel gravitational and electric external fields. The $z = 0$ plane coincides with the free surface of the immovable dielectric layer with thickness h_2 and dielectric constant ε_2. Potential difference $U = U_1 + U_2$, which is a periodic time function, is applied to the capacitor plates. The electric field potential φ is chosen to be zero on the $z = 0$ surface. Let the wave motion on the liquid surface have the characteristic spatial size λ and amplitude a_0. The equation of the free surface is represented in the form $z = \eta(x, y, t)$, where x, y, z, and t are the Cartesian coordinates and time, respectively.

The equations of motion of the fluid and electric field generally have the form

$$\frac{\partial \rho \mathbf{v}}{\partial t} + \mathrm{div}\Pi = \rho \mathbf{g}, \quad \mathrm{div}\mathbf{v} = 0, \tag{1}$$

where

$$\Pi_{ij} = \rho v_i v_j + p\delta_{ij} - \mu\left(\frac{\partial v_i}{\partial x_j} + \frac{\partial v_j}{\partial x_i}\right) - \frac{1}{8\pi}(D_i E_j + D_j E_i) + \frac{1}{8\pi}\mathbf{E}^2\delta_{ij} \tag{2}$$

is the total momentum flux tensor. In our problem, $\mathbf{D} = \varepsilon\mathbf{E}$ and $\mathbf{E} = -\nabla_\varphi$.

The boundary conditions on the free surface $F(x, y, z, t) = z - \eta(x, y, t) = 0$, which is the liquid dielectric–air interface, have the form

$$(\Pi_{1ij} - \Pi_{2ij})n_j = \sigma\left(\frac{1}{R_1} + \frac{1}{R_2}\right)n_i, \quad \frac{\partial F}{\partial t} + (\mathbf{v}, \nabla F) = 0, \quad E_{1\tau} = E_{2\tau}, \quad D_{1n} = D_{2n}. \tag{3}$$

Here, $\mathbf{n}$ is the outward normal to the liquid dielectric surface; subscripts 1 and 2 refer to the region beyond the liquid dielectric and the inner region, respectively; and R_1 and R_2 are the principal curvatures of the free surface. No-slip conditions are imposed on the velocity on the solid surface of the lower electrode, and the electric potential is specified on the lower and upper electrodes as a time function.

We introduce the dimensionless quantities by the expressions

$$x' = \frac{x}{\lambda}, \quad y' = \frac{y}{\lambda}, \quad z' = \frac{z}{h_2}, \quad t' = \frac{t\sqrt{gh_2}}{\lambda},$$

$$\eta(x, y, t) = a_0\eta'(x', y', t'),$$

$$\varphi(x, y, z, t) = U\varphi'(x', y', z', t'),$$

Institute of Thermophysics, Siberian Division, Russian Academy of Sciences, pr. Akademika Lavrent'eva 1, Novosibirsk, 630090 Russia

** e-mail: nick@itp.nsc.ru*

1028-3358/05/5008-0426$26.00

$$u(x, y, z, t) = \sqrt{gh_2}\frac{a_0}{h_2}u'(x', y', z', t'), \quad (4)$$

$$v(x, y, z, t) = \sqrt{gh_2}\frac{a_0}{h_2}v'(x', y', z', t'),$$

$$w(x, y, z, t) = \sqrt{gh_2}\frac{a_0}{h_2}\frac{\lambda}{h_2}w'(x', y', z', t'),$$

$$p(x, y, z, t) = \rho g a_0 p'(x', y', z', t').$$

The problem under consideration is characterized by the set of dimensionless parameters

$$\alpha = \frac{a_0}{h_2}, \quad \beta = \left(\frac{h_2}{\lambda}\right)^2, \quad \zeta = \frac{h_1}{h_2}, \quad J_E = \frac{1}{8\pi}\frac{U^2}{\rho g h_2 h_1^2},$$
$$\mathrm{We} = \frac{\sigma}{\rho g h_2^2}, \quad \mathrm{Ga} = \frac{\sqrt{gh_2}h_2}{\nu}, \quad (5)$$

where J_E is an analog of the Froude number, We is the Weber number, g is the gravitational acceleration, and Ga is the Galileo number. In what follows, we omit primes in the symbols of dimensional quantities.

Seeking the solution of the linearized problem in the form of Fourier series in the homogeneous coordinates x and y:

$$\eta(x, y, t) = Z(t)\exp[i(k_x x + k_y y)],$$

$$w(x, y, z, t) = \sum_{n=0}^{\infty} u_n(t)\cos[\pi n(z+1)] \times \exp[i(k_x x + k_y y)], \ldots,$$

after the cumbersome algebra with inclusion of the boundary and initial conditions, we arrive at the system of two integro-differential equations

$$\ddot{Z}(t) + \frac{\kappa^2}{\mathrm{Ga}\beta^{1/2}}\left[2 + \frac{1}{\cosh\kappa}\right]\dot{Z}(t) + \frac{\kappa\tanh\kappa}{\beta}[1 + \mathrm{We}\kappa^2 - \mathrm{Fr}_E f^2(t)]Z(t)$$
$$= -\frac{1}{\beta\cosh\kappa}\int_0^t\left[\left[\frac{\kappa^2}{\mathrm{Ga}\beta^{1/2}}G_u(t-\tau) + \dot{G}_u(t-\tau)\right]\dot{u}_0(\tau) + \left[\frac{\kappa^2}{\mathrm{Ga}\beta^{1/2}}G_Z(t-\tau) + \dot{G}_Z(t-\tau)\right]\ddot{Z}(\tau)\right]d\tau, \quad (6)$$

$$\dot{u}_0(t) = \frac{1}{\kappa}\tanh\frac{\kappa}{2}\left\{\beta\ddot{Z}(t) - \int_0^t[\dot{G}_u(t-\tau)\dot{u}_0(\tau) + \dot{G}_Z(t-\tau)\ddot{Z}(\tau)]d\tau\right\},$$

where the kernels of the integral operators have the form

$$G_u(t) = 2\kappa^2\sum_{n=1}^{\infty}\left(1 - \exp\left(-\frac{n^2\pi^2 + \kappa^2}{\mathrm{Ga}\beta^{1/2}}t\right)\right) \times \frac{n^2\pi^2}{(n^2\pi^2 + \kappa^2)^2}\frac{\cosh\kappa - (-1)^n}{\cosh\kappa - 1},$$
$$G_Z(t) = 2\beta\kappa\coth\frac{\kappa}{2}\sum_{n=1}^{\infty}\left(1 - \exp\left(-\frac{n^2\pi^2 + \kappa^2}{\mathrm{Ga}\beta^{1/2}}t\right)\right) \times \frac{n^2\pi^2 - \kappa^2}{(n^2\pi^2 + \kappa^2)^2}[1 - (-1)^n], \quad (7)$$

and $\kappa^2 = \beta(k_x^2 + k_y^2)$.

The remaining functions are easily expressed in terms of $Z(t)$ and $u_0(t)$. In particular,

$$u_n(t) = b_n\frac{\kappa^2}{n^2\pi^2 + \kappa^2}u_0(t) + a_n\frac{2\kappa^2}{n^2\pi^2 + \kappa^2}\dot{Z}(t) - \int_0^t\exp\left((-t+\tau)\frac{n^2\pi^2 - \kappa^2}{\mathrm{Ga}\beta^{1/2}}\right) \times \left[b_n\frac{n^2\pi^2}{n^2\pi^2 + \kappa^2}\dot{u}_0(\tau) + a_n\frac{n^2\pi^2 - \kappa^2}{n^2\pi^2 + \kappa^2}\ddot{Z}(\tau)\right]d\tau,$$

where

$$a_n = 2\beta\kappa\coth\frac{\kappa}{2}\frac{[-1 + (-1)^n]}{n^2\pi^2 + \kappa^2},$$

$$b_n = \frac{2\kappa^2}{n^2\pi^2 + \kappa^2}\frac{-(-1)^n + \cosh\kappa}{-1 + \cosh\kappa}.$$

It can be shown that the solutions of system (6) are similar to the Mathieu functions if the time dependence of the electric potential difference on the capacitor plates is harmonic (with frequency Ω). In other words, parametric resonance induced by periodic variation in the electric pressure at the interface between media

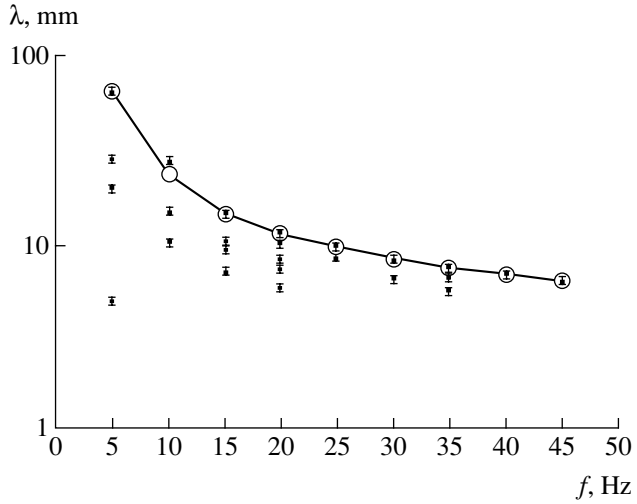

Fig. 1. Wavelength of excited waves vs. the electric field frequency. Open circles are the linear-theory results and closed squares are experimental data for a dielectric (water) 25-mm thick in an electric field of 6 kV.

exists in the electrohydrodynamic system. In the limiting cases of low (Ga $\longrightarrow \infty$) and high (Ga $\longrightarrow 0$) viscosities, as well as for $\kappa \gg 1$, one can derive equations that reduce to the Mathieu equations. In particular, for $\kappa \gg 1$, system (6) reduces to one differential equation

$$Z''(t) + 2\xi Z'(t) + (a - 2q\cos 2t)Z(t) = 0, \qquad (8)$$

where

$$\xi = \frac{\kappa^2}{\Omega \mathrm{Ga}\beta^{1/2}}, \quad a = \omega_0^2(1 + \mathrm{We}\kappa^2) - \frac{\omega_0^2 \mathrm{Fr}_E}{2},$$

$$q = \frac{\omega_0^2 \mathrm{Fr}_E}{4}, \quad \omega_0^2 = \frac{\kappa \tanh \kappa}{\beta},$$

$$\mathrm{Fr}_E = 2\zeta^2\left(\frac{h_2}{\varepsilon_2 h_1 + \varepsilon_1 h_2}\right)^2 \kappa J_E(\varepsilon_1 - \varepsilon_2)$$

$$\times \frac{\varepsilon_1^2(3\varepsilon_2 - 2) + \varepsilon_2^2(1 - 2\varepsilon_1)}{\varepsilon_1 \tanh \kappa + \varepsilon_2 \tanh(\zeta\kappa)}.$$

The substitution $Z(t) = F(t)e^{-\xi t}$ reduces Eq. (8) to the Mathieu equation. For high viscosities (Ga $\longrightarrow 0$), we arrive at an equation similar to Eq. (8), but with different coefficients. In the low-viscosity limit (Ga $\longrightarrow \infty$), the system of equations reduces to one equation in fractional derivatives:

$$Z^{(2)}(t) + d_1 Z^{(3/2)}(t) + (2\zeta + d_2)Z^{(1)}(t)$$
$$+ d_3 Z^{(1/2)}(t) + (a + d_4 - 2q\cos 2t)Z(t) = 0,$$

where d_1, d_2, d_3, and d_4 are given functions of κ.

In the framework of the above complete linear theory of the problem, wave regimes corresponding to the waves observed in the specially conducted experiment were calculated (see Fig. 1). Experimental points below the curve correspond to nonlinear interaction between harmonics. The linear theory agrees with the experimental data within the experimental errors.

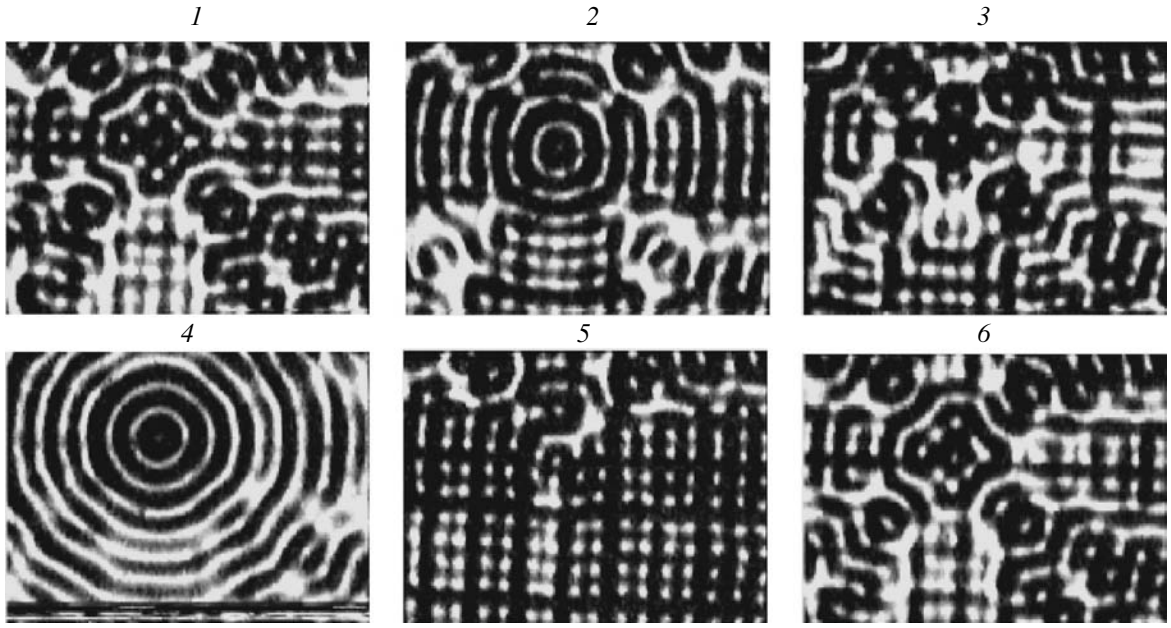

Fig. 2. Shadow patterns of gravity–capillary waves (quasicrystals) on the surface of the distilled water layer 45-mm thick in a 15-Hz ac electric field with an amplitude of 8 kV. The air gap is equal to 4 mm. Wave structures *1–6* are shown.

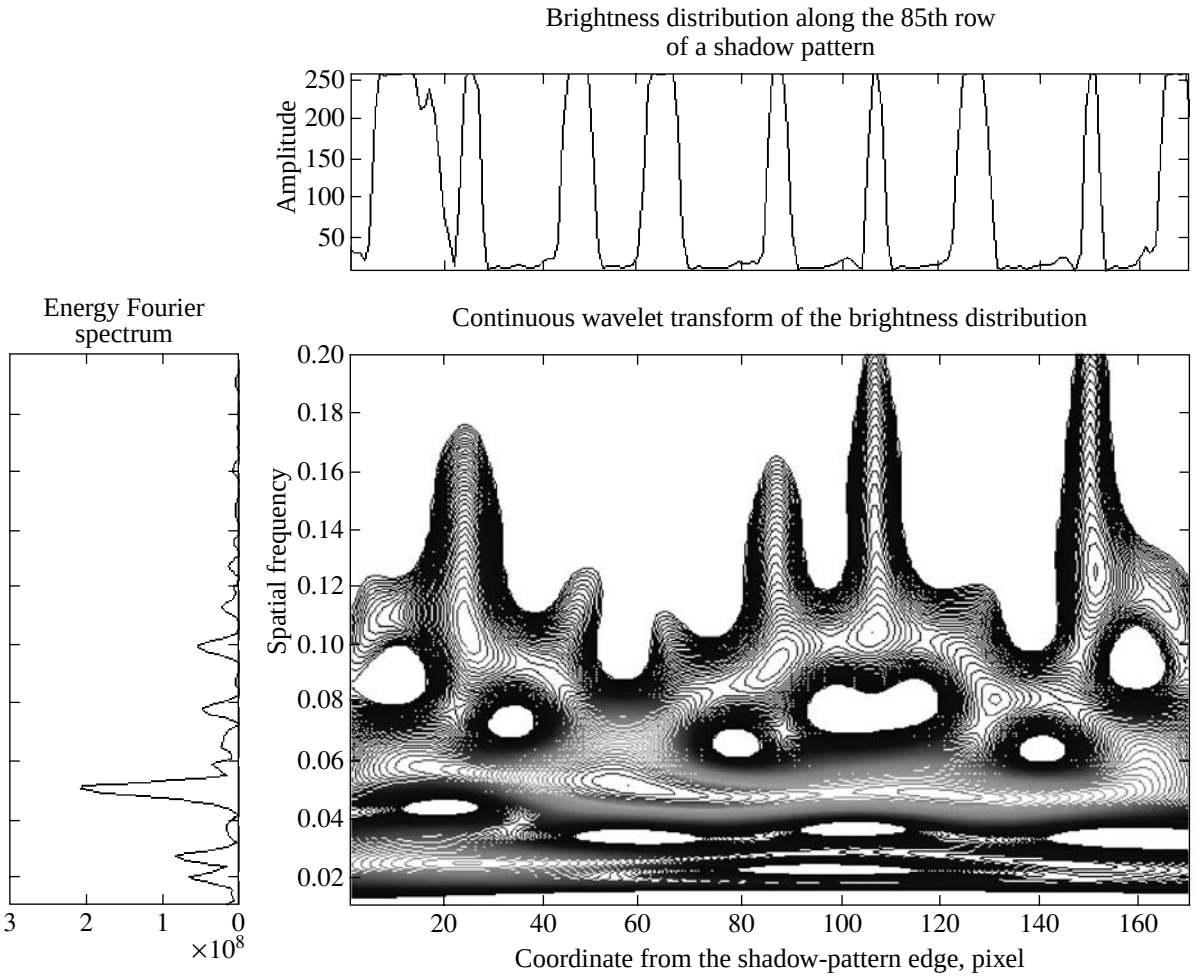

Fig. 3. Wavelet decomposition of the central transverse gravity–capillary wave in a strong oscillating electric field for experimental series no. 3.

In addition to good agreement with the linear theory, the experiment shows that organized dynamic structures, which have recently been referred to as hydrodynamic quasicrystals, arise in such electrohydrodynamic systems [3]. Figure 2 shows an example of these structures. We emphasize that the presented pattern is dynamic, and the shapes of crystals vary periodically in time. Dislocations arise and develop in them, which leads to periodic variation in the structural order. Quasicrystals were visualized using a stroboscope to obtain corresponding shadow patterns of the wave surface of the liquid dielectric. The wave patterns were subjected to additional mathematical processing. Two-dimensional Fourier and wavelet transforms of shadow patterns provide a detailed spectral pattern of wave structures.

The advantages of the new spectral-analysis methods are illustrated in Fig. 3, where the wavelet decomposition of the central transverse gravity–capillary wave in a strong oscillating electric field is shown. This decomposition makes it possible to separate the spatial–frequency modulation in shadow patterns. Figure 3 shows brightness distribution along a certain row of a digital image, as well as two-dimensional spatial Fourier and wavelet spectra. The wavelet spectrum clearly exhibits the spatial–frequency modulation of the large-scale wave component. We note that it would appear to be very difficult to reconstruct such a spatial frequency modulation by other processing methods.

REFERENCES

1. V. A. Briskman and G. F. Shaĭdurov, Dokl. Akad. Nauk SSSR **180** (6), 1315 (1968) [Sov. Phys. Dokl. **13**, 540 (1968)].
2. S. V. Nesterov and S. Ya. Sekerzh-Zen'kovich, Dokl. Akad. Nauk SSSR **256** (2), 318 (1981) [Sov. Phys. Dokl. **26**, 20 (1981)].
3. M. I. Rabinovich and A. B. Ezersky, *Dynamical Theory of Pattern Formation* (Yanus-K, Moscow, 1998) [in Russian].

Translated by R. Tyapaev

Doklady Physics, Vol. 50, No. 8, 2005, p. 430.

ERRATA

Erratum: "Failure of Concrete and Reinforced-Concrete Plates under High-Speed Shock and Explosion" [Doklady Physics 50, 132 (2005)]

S. A. Afanas'ev, N. N. Belov, D. G. Kopanitsa, N. T. Yugov, and A. A. Yugov

In our paper "Failure of Concrete and Reinforced-Concrete Plates under High-Speed Shock and Explosion," the text after the formula $p = A\rho^n + \gamma\rho\varepsilon$ on p. 134 (left column) should be read as "where $\gamma = \gamma_0 + c\rho$, $c = \dfrac{\gamma_H - \gamma_0}{\rho_H}$, A and n are constants, and subscripts 0 and H refer to the ideal gas and state at the Jouguet point, respectively."

Translated by R. Tyapaev

1028-3358/05/5008-0430$26.00